

Clay mineral associations in the clay cap from the Cerro Pabellón blind geothermal system, Andean Cordillera, Northern Chile

S.N. MAZA^{1,*}, G. COLLO^{2,3}, D. MORATA¹, C. LIZANA¹, E. CAMUS¹,
M. TAUSSI⁴, A. RENZULLI⁴, M. MATTIOLI⁴, B. GODOY¹, B. ALVEAR¹,
M. PIZARRO¹, C. RAMÍREZ⁵ AND G. RIVERA^{1,5}

¹ Department of Geology and Andean Geothermal Center of Excellence (CEGA), Facultad de Ciencias Físicas y Matemáticas, Universidad de Chile, Plaza Ercilla 803, Santiago, Chile.

² Universidad Nacional de Córdoba. Facultad de Ciencias Exactas, Físicas y Naturales. Córdoba, Argentina.

³ Consejo Nacional de Investigaciones Científicas y Tecnológicas (CONICET), Centro de investigaciones en Ciencias de la Tierra, (CICTERRA). Córdoba, Argentina.

⁴ Dipartimento di Scienze Pure e Applicate, Università degli Studi di Urbino Carlo Bo, Via Cà le Suore, 2/4 –, 61029 Urbino, Italy.

⁵ ENEL Green Power Chile and Andean countries. Av. Presidente Riesco 5335, 14. Las Condes, Santiago, Chile.

(Received 15 November 2017; revised 28 April 2018; Guest Associate Editor: Blanca Bauluz)

ABSTRACT: The occurrence of smectite-illite and smectite-chlorite minerals series was studied along a thick clay cap (~300 m) drilled in the Cerro Pabellón geothermal field (northern Andes, Chile). X-ray diffraction (XRD) and scanning electronic microscopy (SEM) were used to characterize the alteration mineralogy and clay mineral assemblages and their changes with depth. Cerro Pabellón is a high-enthalpy blind geothermal system, with a reservoir zone from ~500 m to 2000 m depth, with temperatures of 200–250°C. Three main hydrothermal alteration zones were identified: (1) argillic; (2) sub-propylitic, and (3) propylitic, with variable amounts of smectite, illite-smectite, chlorite-smectite, mixed-layer chlorite-corrensite, illite and chlorite appearing in the groundmass and filling amygdalae and veinlets. Chemical and XRD data of smectites, I-S and illites show, with some exceptions, a progressive illitization with depth. The evolution of I-S with depth, shows a sigmoidal variation in the percentage of illite layers, with the conversion of smectite to R1 I-S at ~180–185°C. These temperatures are greater than those reported for other similar geothermal fields and might indicate, at least in part, the efficiency of the clay cap in terms of restricting the circulation of hydrothermal fluids in low-permeability rocks. Our results highlight the importance of a better understanding of clay-mineral evolution in active geothermal systems, not only as a direct (or indirect) way to control temperature evolution, but also as a control on permeability/porosity efficiency of the clay cap.

KEYWORDS: clay minerals, XRD, SEM, clay cap, geothermics, Cerro Pabellón, Andean Cordillera, Chile.

*E-mail: santiagomaz@gmail.com

This paper was presented during the session: 'GG01-Clays in faults and fractures + MI-03 Clay mineral reaction progress in very low-grade temperature petrologic studies' of the International Clay Conference 2017.
<https://doi.org/10.1180/clm.2018.9>

The cap-rock, the heat source, the reservoir and recharge areas are the main four elements in hydrothermal convective geothermal systems. To be effective, a cap-rock should be impermeable enough to maintain the reservoir temperature and the pressure and enthalpy of the system through time (Todesco &

Giordano, 2010; Maffucci *et al.*, 2016; Sánchez-Alfaro *et al.*, 2016). In volcanic and volcanoclastic systems, the development of large, thick cap rocks is favoured by intense argillic alteration which leads to the formation of the clay cap. The efficiency of the clay cap is controlled to a significant extent by the intensity of the hydrothermal alteration, however.

Di- and trioctahedral clay minerals such as smectite, illite, corrensite, chlorite and chlorite-smectite (C-S), chlorite-corrensite (C-Cor) and illite-smectite (I-S) mixed layers are widespread as hydrothermal alteration products (Inoue *et al.*, 2004; Meunier 2005; Stimac *et al.*, 2015). Their formation and transformation to mixed-layer phases (smectite to illite *via* I-S and smectite to chlorite *via* C-S and C-Cor) have been studied widely in many fossil and active hydrothermal systems (Inoue, 1995; Inoue *et al.*, 2004; Meunier *et al.*, 2008a,b; Vázquez *et al.*, 2014; Inoué & Kogure 2016). Moreover, the mixed-layer ordering types and the proportion of illite layers in I-S, as well as the Kübler and Árkai indices, have been employed to constrain the temperatures and conditions (*e.g.* fluid composition, fluid/rock ratio, time) prevailing during the formation of the clay minerals (Kübler, 1968; Środoń, 1981; Merriman & Peacor, 1999; Ji & Browne, 2000; Warr & Ferreiro Mahlmann, 2015; Vidal *et al.*, 2016). Consequently, the study of clay minerals should improve our knowledge of spatial distribution and the relationship with temperature and other factors to estimate the efficiency of the clay cap and its influence on the reservoir zone of the geothermal systems, where other subsurface data are scarce and particularly in the case of blind geothermal systems, where surface thermal manifestations are lacking (*e.g.* Corrado *et al.*, 2014).

The Cerro Pabellón (previously referred to as the ‘Apacheta geothermal project’, Urzúa *et al.*, 2002) might be considered a high-enthalpy blind geothermal field located in the Andean Central Volcanic Zone (CVZ) in northern Chile, at 4500 m a.s.l., ~100 km NE of the city of Calama and ~60 km NNW of El Tatio geothermal field (Fig. 1a). This geothermal field, discovered in 1999 (Urzúa *et al.*, 2002), constitutes the second productive geothermal power plant of South America (Copahue being the first), beginning its operation in 2017. The CVZ is an active volcanic region with heat-flow density values between 50 and 180 mW/m² measured in the active magmatic arc and in the Altiplano (Springer & Forster, 1998). This region comprises abundant Quaternary volcanoes and its geodynamic setting is favourable to the development of several geothermal areas (Aravena *et al.*, 2016).

The purpose of the present study was to examine the vertical distribution of the clay minerals forming the clay cap of the Cerro Pabellón active geothermal field. Our results have allowed us to propose a relationship between the mineral formation-transformation processes and factors such as temperature, fluid–rock composition and time. This represents a contribution to the comprehension of clay-formation processes in blind geothermal systems with the aim of understanding the different mechanism involved during their development.

GEOLOGICAL SETTING

The Andean Central Volcanic Zone (CVZ) has been formed under an intense compressive geodynamic regime since the Early Cretaceous, and is associated with the subduction of the Nazca Plate under the South American Plate, which gives rise to magmatic and hydrothermal activity (*e.g.* Lahsen, 1988; Brasse *et al.*, 2002; Fariás *et al.*, 2005; Charrier *et al.*, 2007; Tassi *et al.*, 2010; Sánchez-Alfaro *et al.*, 2015; Herrera *et al.*, 2017). In northern Chile, the magmatism generated Middle Cretaceous–Late Miocene andesitic to rhyolitic volcanic rocks overlain by Late Miocene–Pleistocene ignimbrite deposits (Lahsen & Trujillo, 1975; Francis & Rundle, 1976; Marinovic & Lahsen, 1984; de Silva, 1989; Ahumada & Mercado, 2009). These volcanic rocks constitute the Altiplano-Puna Volcanic Complex (APVC), a volcano-tectonic silicic magmatic province generated by the partial melt of the thickest continental crust in the world (de Silva, 1989; Schmitz *et al.*, 1999). Over these units, different Pleistocene to Holocene arc volcanoes have been emplaced. The area of the APVC coincides with the surface projection of the Altiplano-Puna Magmatic Body (APMB), a partially molten body within the upper crust, 4 to 25 km below sea level, recognized by geophysical methods (MT, seismic analyses, *etc.*) and interpreted as an incrementally constructed upper-crustal batholith atop an upper crustal MASH zone (Brasse *et al.*, 2002; Zandt *et al.*, 2003; de Silva & Gosnold, 2007; Ward *et al.*, 2014; among others).

In the studied area (Fig. 1b), the CVZ is characterized by several NW–SE oriented eruptive centres dominated by the polygenetic Pleistocene to Holocene Azufre–Inacaliri volcanic range (Trumbull *et al.*, 2006; Rivera *et al.*, 2015), where stratovolcanoes of basaltic andesite to dacitic composition (Apacheta–Aguilucho Volcanic Complex; Ahumada & Mercado, 2009) and rhyolitic domes (Chac-Inca and Pabellón domes; Rivera *et al.*, 2015; Tierney *et al.*, 2016) are recognized

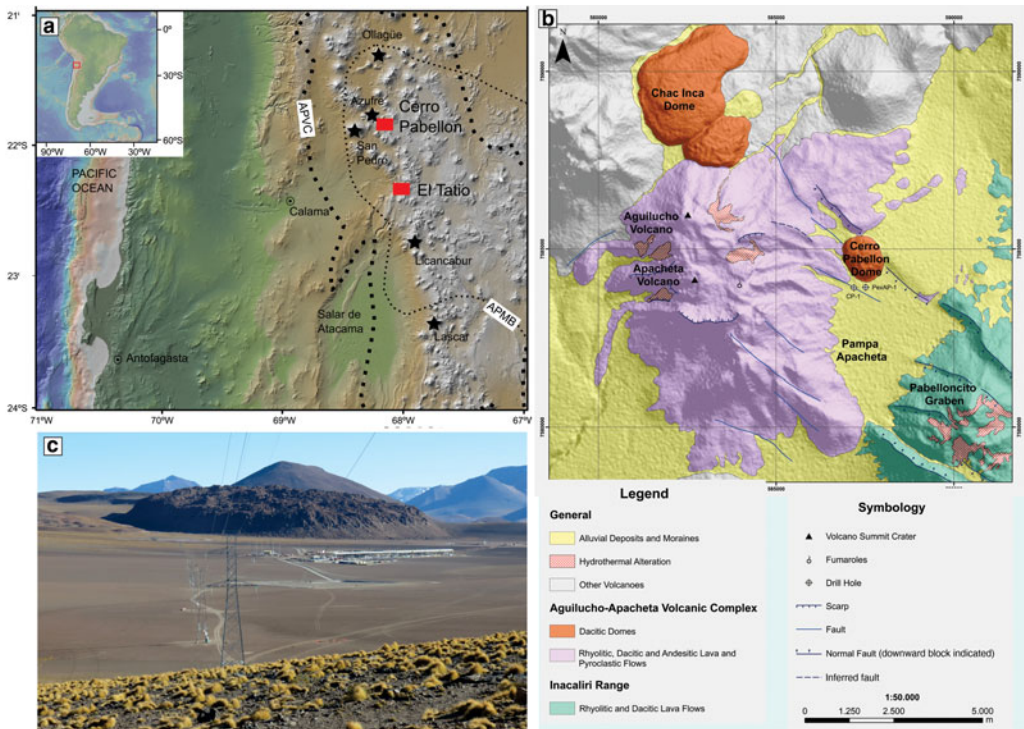


FIG. 1. (a) Central Volcanic Zone (CVZ) in the Andean Cordillera showing the Altiplano-Puna Volcanic Complex (APVC; de Silva, 1989), the main Pleistocene to Holocene volcanoes and the location of the Cerro Pabellón geothermal system; (b) simplified geological map of the Cerro Pabellón geothermal field (modified from Godoy *et al.*, 2017); (c) general view of the Cerro Pabellón geothermal power plant with the 80–130 ka Cerro Pabellón rhyolitic dome in the background.

(Fig. 1b). Locally, the different geological units have been identified by surface geological mapping and recorded from four commercial wells drilled by Geotermia del Norte S. A. (GDN) (Rivera *et al.*, 2015). They mainly correspond to Pliocene–Pleistocene andesitic to dacitic lava, breccias and tuffs, capped by a 100 m-thick welded ash flow, whereas the recent volcanic activity is associated with a series of Pleistocene dacitic lava domes (Pabellón, Chac-Inca and Chanka; Urzúa *et al.*, 2002; Fig. 1b).

A local Pliocene extensional phase, within a regional compressional regime related to the subduction of the Nazca Plate under the South American Plate, took place in the area (e.g. González *et al.*, 2003). This phase generated a NW-striking normal fault system which extends from Azufre volcano in the NW to Inacaliri volcano to the SE (Tibaldi *et al.*, 2016). In the zone investigated, a topographically depressed area of ~100 km² (Tibaldi *et al.*, 2009; Rivera *et al.*, 2015), ~20 km long and 3 km wide, is

well defined by two major faults with converging dips and pronounced scarps (~100–150 m), which form a symmetric graben. This NW–SE graben structure (the Pabelloncito Graben, Francis & Rundle, 1976), affects the NW–SE aligned Pliocene stratovolcanoes. In fact, debris avalanche in the Apacheta-Agulicho volcanic complex (AAVC), located in the northern part of the graben, has recently been interpreted to be triggered by the partial collapse of this volcanic edifice 100–700 ka ago influenced by hydrothermal alteration and the local extensional setting (Godoy *et al.*, 2017). The main NE fault bounding the graben was sealed by the Cerro Pabellón dacitic dome (Tibaldi *et al.*, 2009), 80–130 ka age (⁴⁰Ar/³⁹Ar in biotite, Renzulli *et al.*, 2006; Fig. 1c), the extrusion of which was favoured by the structural weakness related to the normal faults of the graben.

The Cerro Pabellón field does not display surface hydrothermal manifestations; thus it is classified as a blind geothermal field. However, at the summit of Cerro Apacheta volcano (Fig. 1b), two superheated

fumaroles (measured temperatures of 109 and 118°C) with high steam-discharge rates were recognized at 5150 m elevation (Urzúa *et al.*, 2002). The gas geochemistry of these two superheated fumaroles suggests their relationship with a high-temperature geothermal system, with a reservoir composed of biphasic fluids (liquid and vapour), at temperatures of 250–325°C (Urzúa *et al.*, 2002; Tassi *et al.*, 2010). Nevertheless, the only surface alteration related to the active Cerro Pabellón geothermal system is the presence of discontinuous altered clay zones, spatially related to an acid-sulfate alteration, including native sulfur and clay minerals affecting the Pliocene volcanic units (Fig. 1b; Ramírez & Fuente, 1981; Urzúa *et al.*, 2002; Tibaldi *et al.*, 2009).

MATERIAL AND METHODS

Because of the scarcity of surface alteration, this work focused on drill core and cutting samples from two wells provided by GDN for this study: a complete 557 m long exploration drill core (PexAP-1; 21°50′49.68″S, 68°09′21.35″W) and drilling cuttings from the 1821.1 m deep production CP1 well (21°50′56.55″S, 68°09′24.27″W; Figs 1b, 2). Forty-two drilling samples, 25 from the PexAP-1 well and 17 from the CP1 well (Fig. 2), were studied to establish their mineralogical compositions. The samples studied along the PexAP-1 well correspond to depths between 165 and 557 m, with a spacing of ~30 m (Fig. 2), whereas samples along the CP1 well correspond to depths between 425 and 825 m, collected every 25 m. The shallower cuttings, from 175 m to 400 m of depth, studied by Piscaglia (2012), were examined as well. Since the downhole measured temperature at the time of drilling is lower by 10–20°C than the pre-drilling bottom-hole temperatures (*cf.* Artemieva, 2011), pre-drilling temperatures were estimated using the Harrison *et al.* (1983) correction. Samples were studied with optical petrography, X-ray diffraction (XRD) and scanning electron microscopy (SEM). The XRD data were obtained with a Bruker D8 Advance diffractometer with Cu-K α radiation and a Bragg-Brentano geometry at the Department of Physics in the Facultad de Ciencias Físicas y Matemáticas of the Universidad de Chile (Chile) and a Philips PW1830 diffractometer with PW3710 generator and Cu-cathode at 30 mA and 40 kV at the Università degli Studi di Urbino Carlo Bo (Italy). Samples for bulk-rock analysis were dried at room temperature and 10 g samples, powdered in an agate mortar, were examined with XRD at 5–70°2 θ and

interpreted using the *X'Pert Highscore* software. The mineralogy of the <2 μ m fraction was studied only for the samples of the PexAP-1 well, where a continuous core was available. Sample chips were washed in distilled water to remove salts, treated to remove organic matter and calcite, separated by centrifugation and mounted in oriented aggregates following the recommendations of Moore & Reynolds (1997). Clay-mineral analysis was carried out between 2 and 40°2 θ , with a step size of 0.02°2 θ and a scanning time per step of 47.25 s. The minerals in the clay fraction were identified according to the position of the basal reflections of air-dried (AD), ethylene-glycol solvated (EG), and heated to 500°C for 4 h (H) XRD patterns, using the criteria of Moore & Reynolds (1997). Smectite was identified by the peak shift from ~14 Å to 17.5 Å after EG solvation, and collapse to 10 Å after the heat treatment (Moore & Reynolds, 1997). The presence of I-S mixed layers and their illite proportions were determined by the reflection near 16–17°2 θ and the ordering types (R0, R1 and R3) by the position of the reflection from 5 to 8.5°2 θ in AD and EG preparations. Illite was identified by the 10.1 Å, 5.0 Å and 3.33 Å reflections on AD preparations, which are not displaced after the EG and H treatments. Chlorite was identified by the 14, 7, 4.76 and 3.53 Å reflections in AD and EG samples. Mixed-layer chlorite-smectite (C-S), corrensite and C-Cor were identified following the recommendations of Beaufort *et al.* (1997), and Moore & Reynolds (1997).

The Kübler and Árkai indices were determined following the recommendations of Kisch (1991) and Warr & Rice (1994). The values obtained were calibrated to CIS values (Warr & Rice, 1994; Warr & Ferreira Malhmann, 2015; Warr, 2017) through the regression equation: $IK_{CIS} = 0.9192 \times IK + 0.102$. The *b*-parameter was calculated from (060) reflections obtained from thin sections in order to distinguish di- and trioctahedral clay minerals, using XRD traces over the range 50 to 70°2 θ , with a 0.02° step size and 47.25 s counting time.

Six thin rock slides from PexAP-1 well were selected for textural and compositional study of the clay minerals using a FEI Quanta 250 SEM at the Department of Geology in the Facultad de Ciencias Físicas y Matemáticas of the Universidad de Chile (Chile). Samples were carbon coated and examined through backscattered electron (BSE) images. Energy dispersive X-ray spectrometry (EDS) analyses were performed on selected regions to obtain semi-quantitative clay-mineral compositions. For BSE and EDS the operating conditions were 15 keV accelerating

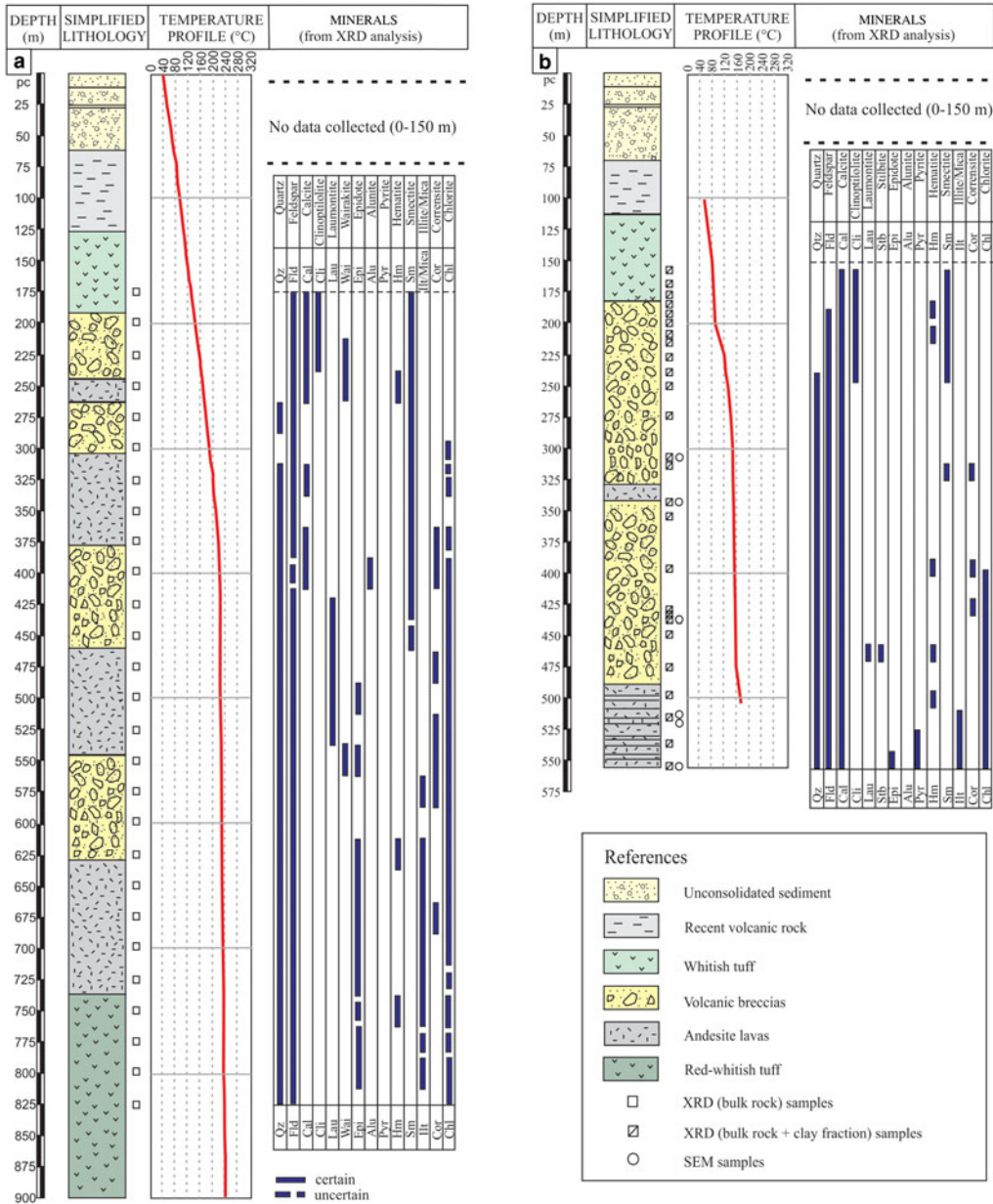


FIG. 2. Simplified lithological columns of the Cerro Pabellón geothermal field obtained from the CP-1 (a) and the PexAP-1 (b) wells, showing measured temperature profiles (°C) and the main alteration minerals identified through petrography and bulk-rock XRD.

voltage, a spot size of 5 μm, working distance of 10 mm, and a counting time of 60 s. The structural formulae of dioctahedral smectites, mixed-layer I-S and illites were calculated considering 22 oxygen

atoms. A 0.80 Fe³⁺/Fe_{tot} ratio was taken into consideration until the depth of 450 m given the presence of hematite, while for the samples from deeper levels, a ratio of 0.4 Fe³⁺/Fe_{tot} was used given

the presence of pyrite, ilmenite, chalcopyrite and galena (Guidotti *et al.*, 1994). The structural formulae of C-S and Cor were calculated considering 25, whereas C-Cor and chlorite were calculated considering 14 oxygens. A 0.20 $\text{Fe}^{3+}/\text{Fe}_{\text{tot}}$ ratio was assumed for these phases (Inoue *et al.*, 2010).

RESULTS

Mineral paragenesis

Petrography and whole-rock XRD analysis. The stratigraphic sequence of both wells is summarized in Fig. 2. The different lithologies recorded from PexAP-1 and CP1 wells are comparable (Rivera *et al.*, 2015): the first ~190 m consist of unconsolidated sediments (0–65 m), recent volcanic rocks (65–125 m) and whitish tuffs (125–190 m); from ~190 to 737 m the sequence is characterized by an alternation of breccias and andesitic lavas; from ~737 to 900 m red-whitish tuffs were recognized. Finally, from 900 to 1755 m a series of andesitic-dacitic lavas with intercalations of tuffs were distinguished. Secondary alteration minerals were studied in the continuous drill core PexAP-1 well and in the cuttings from the CP1 well (Fig. 2). Macroscopic and microscopic analyses of the drill core (PexAP-1) show that the andesitic rocks display intense and pervasive hydrothermal alterations, with the primary mineralogy being replaced completely, represented by sparse relicts of zoned and poly-synthetic twinned plagioclase and clinopyroxene accompanied by scarce amphibole, biotite and olivine relicts. In general Na-Ca-plagioclase phenocrysts have been partly to completely dissolved and pseudomorphically replaced by Na-plagioclase and K-feldspar or by clay minerals. Primary mafic minerals are mostly pseudomorphed and replaced by clay minerals associated with hematite and variable amounts of quartz. At least two different microtextural types of veinlets, filled by quartz + calcite ± chlorite, were recognized (Fig. 3a–c) suggesting an intense, hot fluid–rock interaction. Rhombic calcite crystals, present in the centres of veinlets and vesicles, are overgrown by quartz displaying crustiform, colloform, zonal and mosaic (or jigsaw) textures. The proportions of clay minerals in veinlets are variable. Sparse relict amygdals, clast outlines, trachytic textures and brecciation features were preserved.

Similar mineral assemblages were recognized from XRD analyses along both wells (Fig. 2). Smectite is the main clay mineral in the ~165–250 m interval which is also characterized by the absence of quartz and the

presence of clinoptilolite (Fig. 3d), calcite and hematite. From ~250 to 400 m, mixed-layer I-S and C-S linked to albite, calcite, hematite, quartz, stilbite and laumontite were identified. From ~400 m, chlorite is intimately associated with hematite, adularia, albite, calcite, quartz, epidote, while illite was identified from ~510 m. The Ca-zeolites (clinoptilolite-stilbite-laumontite-wairakite sequence) are present from 165 m in a relatively discontinuous way, mainly filling vesicles and voids (Fig. 3b). From ~475 m, it is possible to recognize epidote, sporadically at first and then more often from 625 m.

Clay mineralogy

XRD of the <2 μm fraction. The clay minerals identified in the PexAP-1 well were smectite, I-S, illite, C-S, corrensite, C-Cor and chlorite, showing a zonation with depth (Fig. 4, Table 1). Smectite is present continuously from the shallower parts of the borehole down to a depth of 251 m and reappears at a depth of 319 m (Table 1, Figs 2, 4a). At greater depths, smectite disappears and is replaced by mixed-layer I-S: R0-type I-S with ~10% illite layers at 346 m depth, R1-type I-S with 55–66% illite layers at ~433 m and R3-type I-S with >90% illite layers occurring continuously from depths of ~451 to ~493 m. Then, to the bottom of the well, R3 I-S (>90% illite) was identified.

Samples CP273 and CP401 contain R3-type I-S with illite contents which are not in agreement with those from the nearby samples. Mixed-layer C-S appears together with smectite in shallower levels between 213 and 346 m (Fig. 4a). Corrensite is also present discontinuously with R1 and R3-type I-S between 273 (Fig. 4b) and 434 m depth, whereas from 400 m to the bottom of the well, mixed-layer C-Cor coexists with chlorite and illite (Fig. 4c).

Kübler (KI) and Árkai indices. The $\text{KI}_{(\text{CIS})}$ for illite-bearing samples from depths of 534 and 557 m (CP534 and CP557) shows a value of $0.70^\circ\Delta 2\theta$ for AD samples and values of 0.80 and $0.71^\circ\Delta 2\theta$ for EG samples (Table 2), indicative of temperatures of <200°C (diagenetic field) in sedimentary basins (Warr & Ferreira Mahlmann, 2015). The small differences between the AD and EG preparations and the asymmetric form of the peak suggest illite interlayering with small amounts of R3-type I-S. Chlorite-bearing samples between depths of 534 and 557 m show Árkai indexes of 0.38 and $0.40^\circ\Delta 2\theta$ for AD preparations and of $0.46^\circ\Delta 2\theta$ for EG preparations. The small variation between AD and EG preparations indicates that the

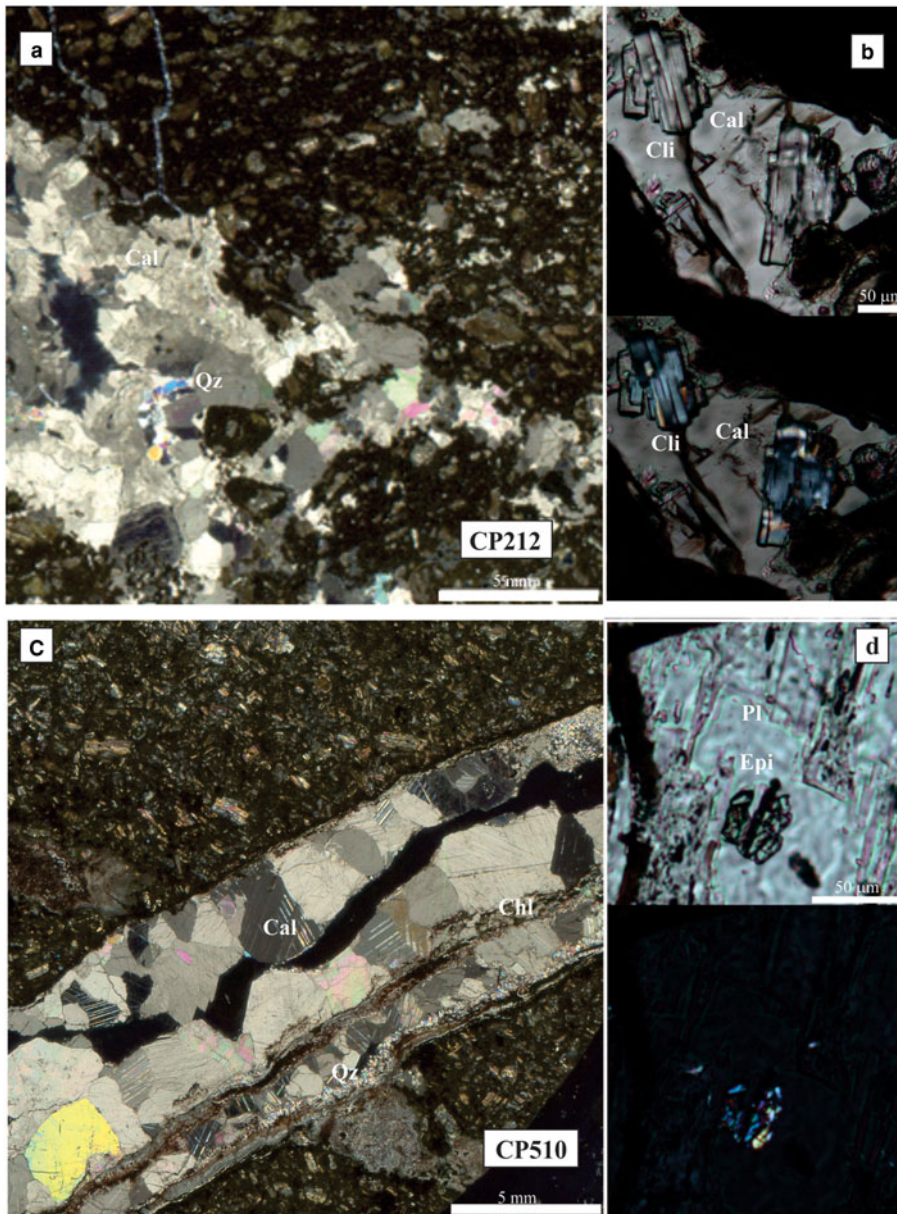


FIG. 3. Photomicrographs of representative samples taken from the shallow and deep zones from PexAP-1 well. Cal: calcite; Qz: quartz; Cli: clinoptilolite; Epi: epidote. (a) Sample located at 212 m depth. Vein filled by zeolites, rhombic calcite, zonal and flamboyant quartz. The matrix has been replaced by clays minerals; (b) plane polarized and crossed polarized light photomicrographs showing clinoptilolite followed by rhombic calcite; (c) vein in sample located at 552 m depth consisting of Fe oxides and jigsaw and zonal quartz; (d) plane polarized and crossed polarized light photomicrographs of a sample located at 510 m depth. Plagioclase phenocryst replaced by epidote.

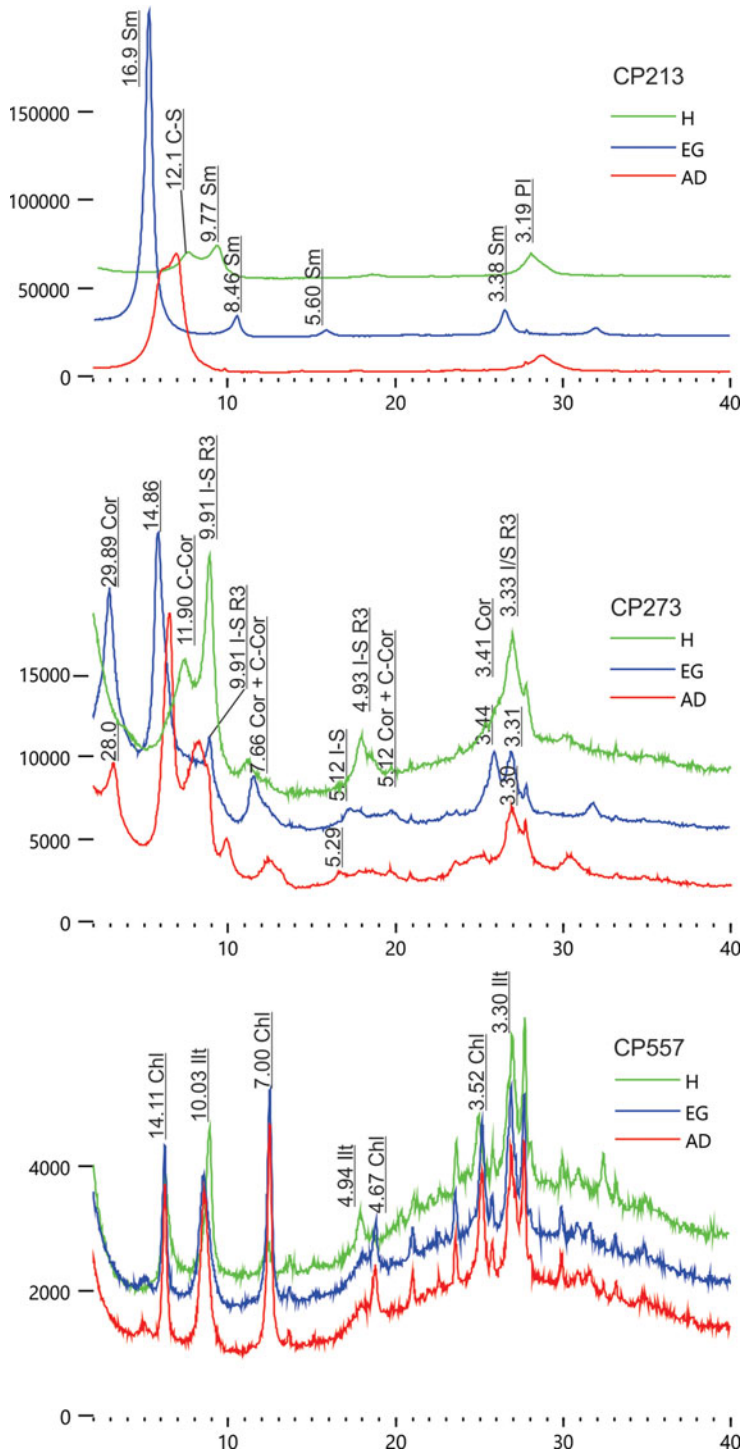


FIG. 4. XRD patterns in the <2 μm fraction of representative samples in the PexAP-1 well. Red: air dried; blue: after ethylene glycol solvation; green: heated at 500°C.

TABLE 1. Clay mineralogy of the PexAP-1 well. Sm: smectite; I-S: illite-smectite; Ilt: illite; C-S: chlorite-smectite; Cor: corrensite; C-Cor: chlorite-corrensite; Chl: chlorite. % of illite in I-S and *in situ* measured temperature are also shown.

Sample	Clay minerals									
	T (°C)	Sm	(R0) I-S	(R1) I-S	(R3) I-S	Ilt	C-S	Cor	C-Cor	Chl
CP165	95	x								
CP170	97	x								
CP173	100	x								
CP181	103	x								
CP184	106	x								
CP197	110	x								
CP212	117	x								
CP213	124	x					x			
CP228	141	x					x			
CP240	148	x					x			
CP251	154	x					x			
CP273	172				88			x	x	
CP313	173	x					x			
CP319	173	x					x			
CP346	176		10				x			
CP401	180				85			x	x	x
CP432	183			56					x	x
CP433	183			64				x	x	x
CP434	183			66				x	x	x
CP451	184				80				x	x
CP467	185				90				x	x
CP494	190				90				x	x
CP512	208					x			x	x
CP534	222					x			x	x
CP557	238					x			x	x

presence of expandable layers in chlorite is negligible. The values obtained for Árkai indices are smaller than the $\text{KI}_{(\text{CIS})}$ values obtained for the same samples.

Chlorite, white mica and smectite *b*-parameters

The positions of d_{060} reflections for the samples studied from the top to the bottom of the well are

shown in Fig. 5. For samples included within the interval recording mainly smectites, mixed-layer I-S and C-S (from CP313 to CP434), the d_{060} spacings are 1.485–1.552 Å (Fig. 5), which correspond to *b*-parameter values of 8.91–9.312 Å consistent with the presence of both di- and trioctahedral phases (Beaufort *et al.*, 1997; Nieto, 1997; Moore & Reynolds, 1997; Meunier, 2005). In the samples from shallower depths,

TABLE 2. Kübler and Árkai index values of the samples from the PexAP-1 well.

	FWHM (°2 θ)		$\text{IK}_{(\text{CIS})}$		FWHM (°2 θ)		AI	
	AD	EG	AD	EG	AD	EG	AD	EG
CP534	0.67	0.80	0.70	0.80	0.32	0.39	0.38	0.46
CP557	0.65	0.66	0.70	0.71	0.39	0.39	0.40	0.46

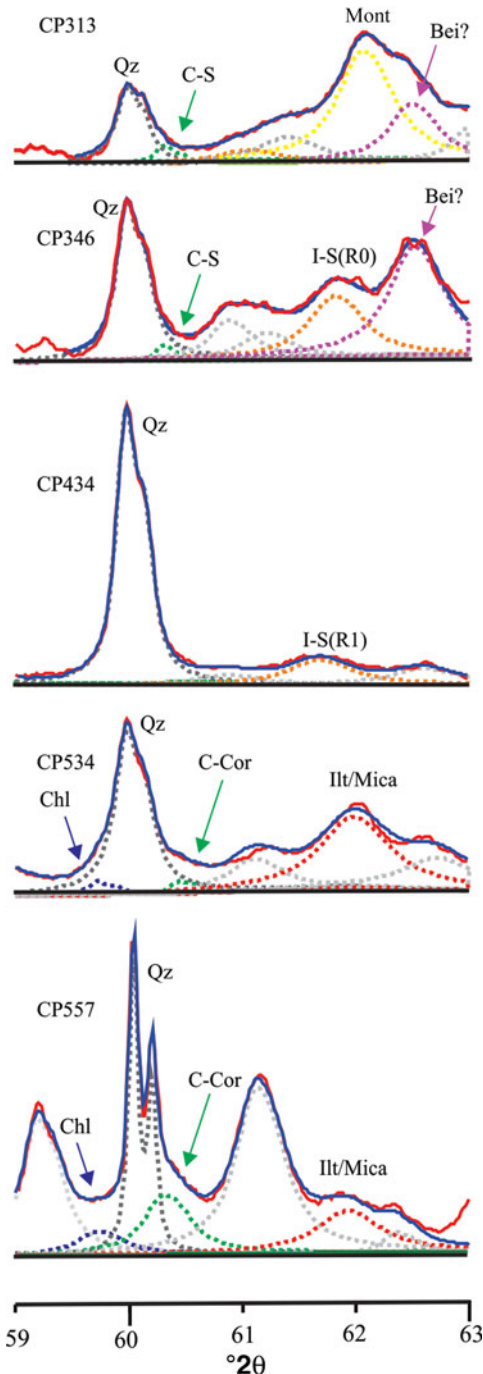


FIG. 5. Positions of d_{060} spacing for the studied samples from top to bottom of the PexAP-1 well. Sample numbers indicate depth below surface. Mont: montmorillonite; Bei: beidellite; Qz: quartz; C-S: chlorite-smectite; C-Cor: chlorite-corrensite; Ilt: illite; I-S: illite-smectite; Chl: chlorite.

the b parameters are consistent with dioctahedral smectites and minor mixed-layer C-S (8.94 and 9.18 Å, respectively). The change of b parameters from ~ 8.94 Å (montmorillonite) towards 9.00 Å from CP313 to CP346 to CP434 might be related to the progressive appearance of R0 and R1-type I-S (Fig. 5). Reflections at 1.486 Å (b parameter = 8.92 Å) might be associated with the presence of some beidellitic compositions. For samples in the depth interval 534–557 m the b parameters indicate the occurrence of chlorite-bearing mixed layers (~ 9.3 and 9.18 Å, respectively) and dioctahedral micas (8.98 and 9.00 Å; Moore & Reynolds, 1997; Nieto, 1997; Chemtob et al., 2015).

Scanning electron microscopy

Typical SEM textures from each zone are shown in Figs 6 and 7. In the sample representative of the shallowest zone (CP313), widespread smectite replaces plagioclase, mafic phenocrysts and groundmass, or appears filling veins and showing a curved-lens morphology without preferred orientation (Fig. 6a,b). Moreover, smectite occurs filling small dissolution voids inside relict plagioclase and ferromagnesian minerals, showing a slightly crenulated to ribbon-like morphology, associated with Fe oxides and quartz, confirming an intense pervasive alteration (Gifkins et al., 2005). At 346 m depth (CP346, Fig. 6c,d) the clay minerals identified were mixed-layer I-S and C-S, with morphologies similar to those described for smectite in CP313. The C-S shows way to ribbon-like morphology; it appears filling veins or vesicles surrounded by thin ribbons of filamentous mixed-layer I-S (500–800 nm) and rimmed by quartz. Calcite is very frequent in veins surrounded by haloes of I-S and quartz (sample CP434, Fig. 6e,f). Mixed-layer C-S also appears as thin ribbons with a filamentous morphology; these were differentiated from I-S by their lighter grey tone, due to the greater average atomic number (Fig. 6c,d). From 510 m downwards, authigenic illite grows on phenocryst dissolution voids and veins showing a ribbon morphology, frequently in contact with chlorite (sample CP510, Fig. 7a–c). Chlorite forms clusters of ~ 1 μm long crystals, also filling voids (sample CP557; Fig. 7d). Phenocrysts replaced by illite and chlorite show titanite rims (Fig. 7d). Adularia (Fig. 7c) and sulfides, mainly pyrite, chalcopyrite and galena, appear from a depth of ~ 470 m, together with a decrease in Fe oxides, probably indicating a change in redox conditions.

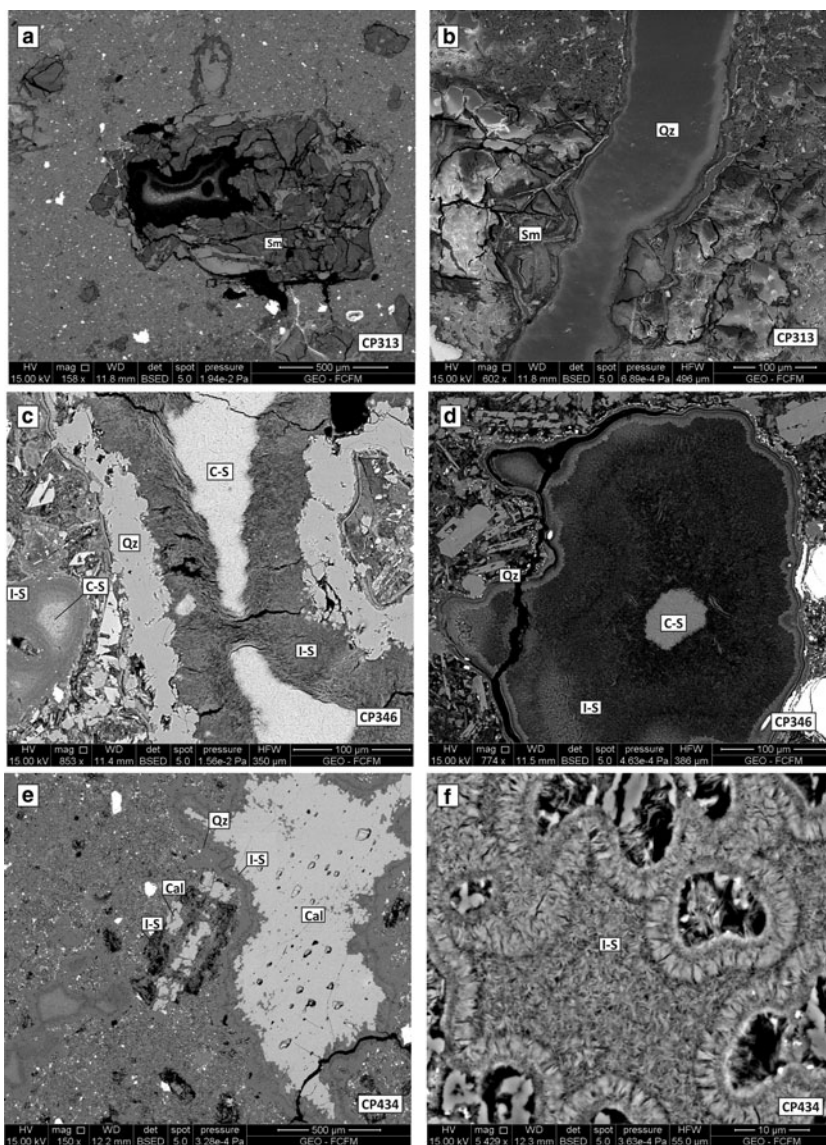


FIG. 6. Representative BSE images obtained using SEM from samples of the PexAP-1 well. (a) Slightly crenulated to ribbon-like smectite replacing plagioclase phenocrysts and the groundmass, associated with quartz and hematite; (b) vein consisting of quartz cross-cutting a smectitic matrix; (c) wavy to ribbon-like morphology of C-S filling veins and vesicles surrounded by thin ribbons of filamentous mixed-layer I-S and quartz rims; (d) vesicle consisting of mixed-layer C-S and I-S; (e) I-S and calcite replacing phenocryst and filling vesicle; (f) detail of (e) showing I-S ribbon-like morphology. Sm: smectite; Cal: calcite; C-S: chlorite-smectite; I-S: illite-smectite; Qz: quartz.

Chemical compositions

Diocahedral clays. The structural formulae calculated from semi-quantitative EDS analysis corresponding to smectite, mixed-layer I-S and illite, which are compatible with dioctahedral types in all cases, with

$\sum_{\text{oct}} \sim 2$ a.p.f.u, are shown in Table 3. The shallowest sample (CP313), which consists mainly of smectites, according to XRD data, contains the most Si^{4+} and Mg^{2+} , reflecting a montmorillonitic composition (Fig. 8), with Ca^{2+} and K^{+} being the major interlayer

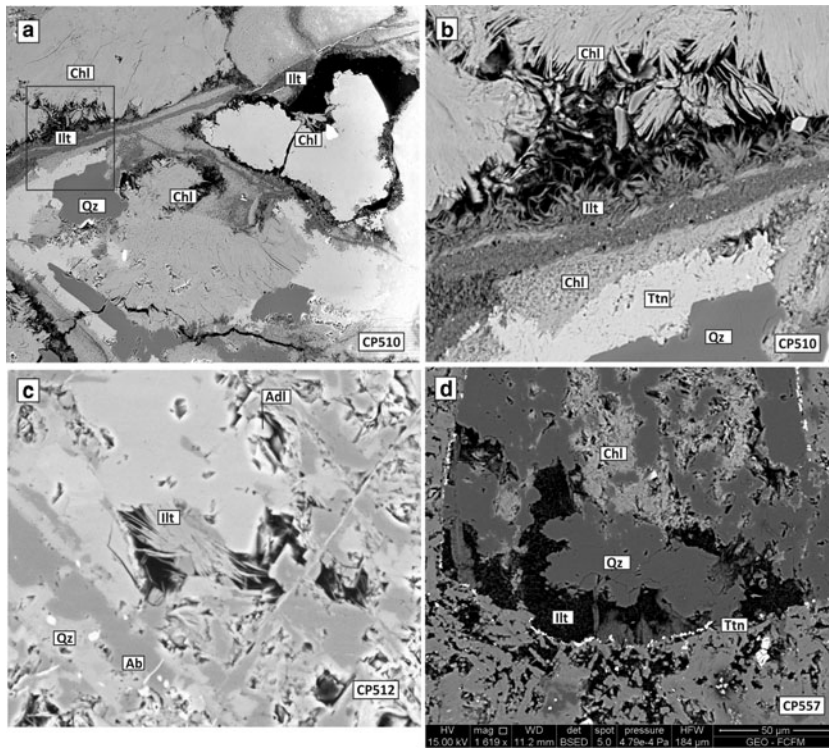


FIG. 7. Representative BSE images obtained using SEM from samples of the PexAP-1 well. (a) Cluster of elongate chlorite in contact with illite; (b) detail of (a) showing ribbon morphology of illite in void and vein; (c) voids filled with filamentous illite and with quartz, albite and adularia crystals; (d) primary phenocrysts replaced by chlorite and illite with titanite rims. Qz: quartz; Illt: illite; Tnt: titanite; Chl: chlorite; Adl: adularia; Ab: albite.

cations (0.41–0.59 a.p.f.u.). The presence of low octahedral occupancies in some places (Table 3) might indicate a mixture of dioctahedral clay minerals with other silicates from the matrix, e.g. quartz. In deeper samples (~346 m), where R0 I-S type is the main dioctahedral clay mineral, there is an increase in the Al^{3+} and K^+ contents and a decrease in Si^{4+} and Ca^{2+} and a net increase in the interlayer charge (0.37–0.79 a.p.f.u.), which might be associated with the increase in illite layers in I-S (Figs 9, 10). The same trend was observed for samples with R1 I-S type and illites until a depth of 557 m. At a depth of 434 m, with prevailing R1 I-S, K^+ is the dominant interlayer cation, with values varying between 0.65 and 0.77 a.p.f.u., and interlayer charges between 0.74 and 0.96 a.p.f.u. Between depths of 510 and 512 m, K^+ ranges between 0.64 and 0.94 a.p.f.u., whereas interlayer charges are between 0.64 and 0.99 a.p.f.u., in accordance with the illite identified by XRD.

The Fe + Mg content is greater in smectite and R0 I-S from samples CP313 and CP346 than in R1 I-S and illite until the depth of 557 m (Table 3; Fig. 10b). However, the deepest samples (557 m) do not follow this trend due to an increase in Si, Fe and Mg values and a decrease in Al (Fig. 10).

Trioctahedral clays. The structural formulae of chlorite-bearing mixed-layer phases are shown in Table 4. The relationships between M^+ -Si- and R^{2+} cations are shown in Fig. 11. Trioctahedral clays from sample CP346 show compositions compatible with mixtures between pure chlorite and corrensites, as they depict lower Si/(Si + Al) ratios, interlayer charges and greater octahedral occupancies than corrensites. The Mg contents are greater than those of Fe and the main interlayer cation is Ca. At a depth of ~434 m (CP434), K^+ is the main interlayer cation. From ~510 m depth downwards, the Fe^{2+} contents are greater than the Mg^{2+} contents in trioctahedral phases, consistent with the

TABLE 3. EDS analyses of smectites, mixed-layer I-S and illites normalized to O₁₀(OH)₂.

	Si	Al ^{IV}	Al ^{VI}	Fe	Mg	Mn	Ti	∑ oct	K	Na	Ca	∑ int	Al Tot
CP313-1*	3.83	0.17	1.16	0.56	0.37	0.00	0.00	2.08	0.07	0.09	0.12	0.41	1.33
CP313-3*	3.82	0.18	1.16	0.33	0.59	0.00	0.00	2.08	0.45	0.14	0.00	0.58	1.34
CP313-4*	3.97	0.03	0.86	0.57	0.62	0.00	0.00	2.06	0.50	0.09	0.00	0.59	0.89
CP346-1**	3.91	0.09	1.34	0.30	0.25	0.00	0.00	1.90	0.22	0.00	0.24	0.71	1.43
CP346-2**	3.79	0.21	1.20	0.47	0.30	0.00	0.00	1.98	0.38	0.00	0.15	0.68	1.41
CP346-3**	3.83	0.17	1.38	0.26	0.26	0.00	0.00	1.90	0.05	0.00	0.37	0.79	1.55
CP346-4**	3.92	0.08	1.42	0.27	0.24	0.00	0.00	1.93	0.11	0.00	0.23	0.57	1.5
CP346-5**	3.92	0.08	1.41	0.28	0.24	0.00	0.00	1.93	0.00	0.00	0.28	0.56	1.49
CP346-6**	3.92	0.08	1.44	0.28	0.27	0.00	0.00	1.99	0.00	0.00	0.22	0.44	1.52
CP346-7**	3.88	0.12	1.22	0.49	0.29	0.00	0.00	2.00	0.16	0.00	0.17	0.50	1.34
CP346-8**	3.71	0.29	1.08	0.60	0.30	0.00	0.00	1.98	0.40	0.00	0.19	0.78	1.37
CP346-9**	3.78	0.22	1.18	0.53	0.26	0.00	0.00	1.97	0.27	0.00	0.20	0.68	1.4
CP346-10**	3.73	0.27	1.32	0.36	0.27	0.00	0.00	1.96	0.48	0.08	0.10	0.75	1.59
CP346-11**	3.91	0.09	1.34	0.41	0.27	0.00	0.00	2.02	0.10	0.07	0.10	0.37	1.43
CP346-12**	3.81	0.19	1.24	0.48	0.35	0.00	0.00	2.06	0.11	0.00	0.17	0.45	1.43
CP346-13**	3.91	0.09	1.34	0.30	0.25	0.00	0.00	1.90	0.22	0.00	0.24	0.71	1.43
CP346-14**	3.79	0.21	1.20	0.47	0.30	0.00	0.00	1.98	0.38	0.00	0.15	0.58	1.41
CP346-15**	3.83	0.17	1.38	0.26	0.26	0.00	0.00	1.90	0.05	0.00	0.37	0.79	1.55
CP434-1**	3.52	0.48	1.44	0.32	0.18	0.00	0.00	1.95	0.70	0.00	0.13	0.96	1.92
CP434-2**	3.59	0.41	1.34	0.42	0.20	0.00	0.00	1.96	0.73	0.00	0.09	0.91	1.75
CP434-3**	3.55	0.45	1.47	0.31	0.18	0.00	0.00	1.96	0.65	0.00	0.11	0.86	1.92
CP434-4**	3.60	0.40	1.33	0.44	0.26	0.00	0.00	2.03	0.74	0.00	0.00	0.74	1.73
CP434-5**	3.57	0.43	1.28	0.47	0.25	0.00	0.00	2.01	0.72	0.00	0.06	0.85	1.71
CP434-6**	3.59	0.41	1.12	0.63	0.26	0.00	0.00	2.01	0.77	0.00	0.06	0.89	1.53
CP510-1***	3.51	0.49	1.74	0.10	0.18	0.00	0.00	2.01	0.67	0.00	0.00	0.67	2.23
CP510-2***	3.55	0.45	1.66	0.14	0.22	0.00	0.00	2.02	0.68	0.00	0.00	0.68	2.11
CP510-3***	3.49	0.51	1.78	0.08	0.14	0.00	0.00	2.00	0.67	0.00	0.00	0.67	2.29
CP510-4***	3.50	0.50	1.80	0.06	0.13	0.00	0.00	1.99	0.68	0.00	0.00	0.68	2.3
CP510-5***	3.43	0.57	1.58	0.20	0.33	0.00	0.00	2.11	0.64	0.00	0.00	0.64	2.15
CP510-6***	3.53	0.47	1.63	0.16	0.23	0.00	0.00	2.01	0.72	0.00	0.00	0.72	2.1
CP512-1***	3.40	0.60	1.60	0.25	0.13	0.00	0.00	1.98	0.88	0.00	0.00	0.88	2.2
CP512-2***	3.47	0.53	1.57	0.27	0.13	0.00	0.00	1.96	0.88	0.00	0.00	0.88	2.1

(continued)

TABLE 3. (contd.)

	Si	Al ^{IV}	Al ^{VI}	Fe	Mg	Mn	Ti	Σ oct	K	Na	Ca	Σ int	Al Tot
CP512-3***	3.37	0.63	1.59	0.26	0.13	0.00	0.00	1.98	0.93	0.00	0.00	0.93	2.22
CP512-4***	3.37	0.63	1.58	0.27	0.12	0.00	0.00	1.97	0.94	0.00	0.00	0.94	2.21
CP512-5***	3.53	0.47	1.58	0.21	0.12	0.00	0.00	1.91	0.93	0.00	0.00	0.93	2.05
CP512-6***	3.43	0.57	1.63	0.19	0.10	0.00	0.00	1.92	0.85	0.14	0.00	0.99	2.2
CP512-7***	3.39	0.61	1.73	0.14	0.08	0.00	0.00	1.95	0.89	0.00	0.00	0.89	2.34
CP512-8***	3.41	0.59	1.63	0.21	0.12	0.00	0.00	1.95	0.93	0.00	0.00	0.93	2.22
CP512-9***	3.41	0.59	1.67	0.20	0.11	0.00	0.00	1.97	0.86	0.00	0.00	0.86	2.26
CP512-10***	3.47	0.53	1.65	0.18	0.15	0.00	0.00	1.98	0.82	0.00	0.00	0.82	2.18
CP512-11***	3.45	0.55	1.62	0.22	0.12	0.00	0.00	1.95	0.90	0.00	0.00	0.90	2.17
CP512-12***	3.41	0.59	1.69	0.20	0.10	0.00	0.00	1.99	0.81	0.00	0.00	0.81	2.28
CP557-1***	3.57	0.43	1.48	0.28	0.18	0.00	0.00	1.93	0.92	0.00	0.00	0.92	1.91
CP557-2***	3.58	0.42	1.35	0.39	0.20	0.00	0.00	1.94	0.97	0.00	0.00	0.97	1.77
CP557-3***	3.64	0.36	1.35	0.37	0.18	0.00	0.00	1.91	0.97	0.00	0.00	0.97	1.71
CP557-4***	3.62	0.38	1.41	0.32	0.20	0.00	0.00	1.92	0.94	0.00	0.00	0.94	1.79
CP557-5***	3.57	0.43	1.35	0.39	0.22	0.00	0.00	1.96	0.94	0.00	0.00	0.94	1.78
CP557-6***	3.60	0.40	1.32	0.43	0.23	0.00	0.00	1.98	0.87	0.00	0.00	0.87	1.72
CP557-7***	3.57	0.43	1.27	0.47	0.24	0.00	0.00	1.98	0.92	0.00	0.00	0.92	1.7

* Sm; ** I-S; *** illite.

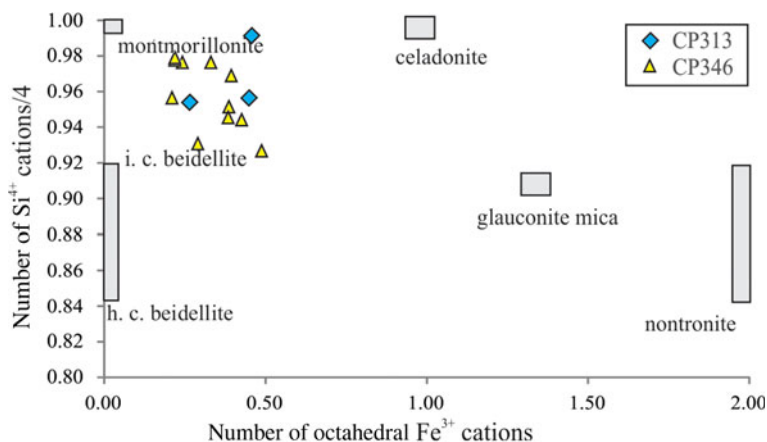


FIG. 8. Compositional diagram (number of octahedral Fe^{3+} vs. number of Si^{4+} cations/4 in a.p.f.u.) for the smectitic samples. Sample CP346, with I-S (R0) was also included.

b -parameter values ($\sim 9.3 \text{ \AA}$) that might be associated with chamositic chlorites (Nieto, 1997). Although the XRD analyses show that from depths of 451 m downwards there is a chlorite-rich domain, high Si^{4+} contents and interlayer charges up to 0.28 (K^+ , Ca^{+2}) emphasize the presence of variable amounts of C-Cor (also identified through XRD; Table 1) and/or fine intergrowths of chlorite with other phyllosilicates (e.g. illite) below the resolution of EDS.

DISCUSSION

Distribution of secondary minerals and compositional evolution of clay minerals with depth

The present study differentiates several mineral assemblages down the wells that may be grouped into three main hydrothermal alteration zones (Fig. 12): (1)

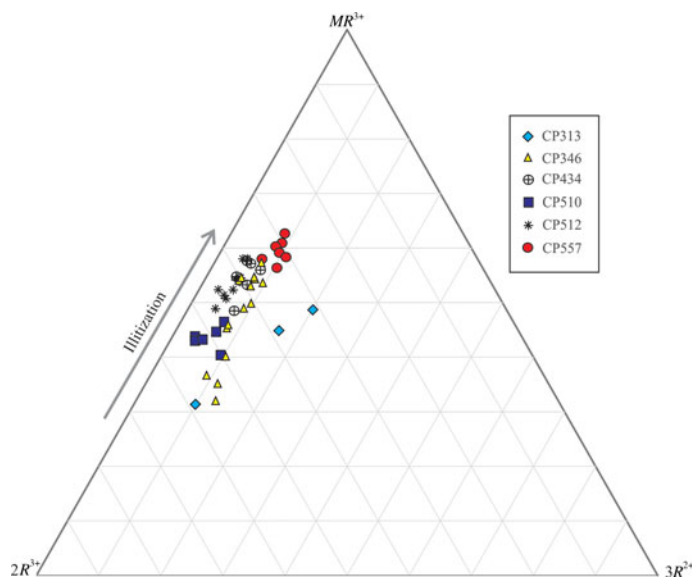


FIG. 9. MR^{3+} - 2R^{3+} - 3R^{2+} diagram (Velde, 1985) showing the compositional evolution of smectite, I-S and illite. MR^{3+} : $\text{Na}^+ + \text{K}^+ + 2\text{Ca}^{2+}$; 2R^{3+} : $(\text{Al}^{3+} + \text{Fe}^{3+} - \text{MR}^{3+})/2$; 3R^{2+} : $(\text{Fe}^{2+} + \text{Mg}^{2+} + \text{Mn}^{2+})/3$.

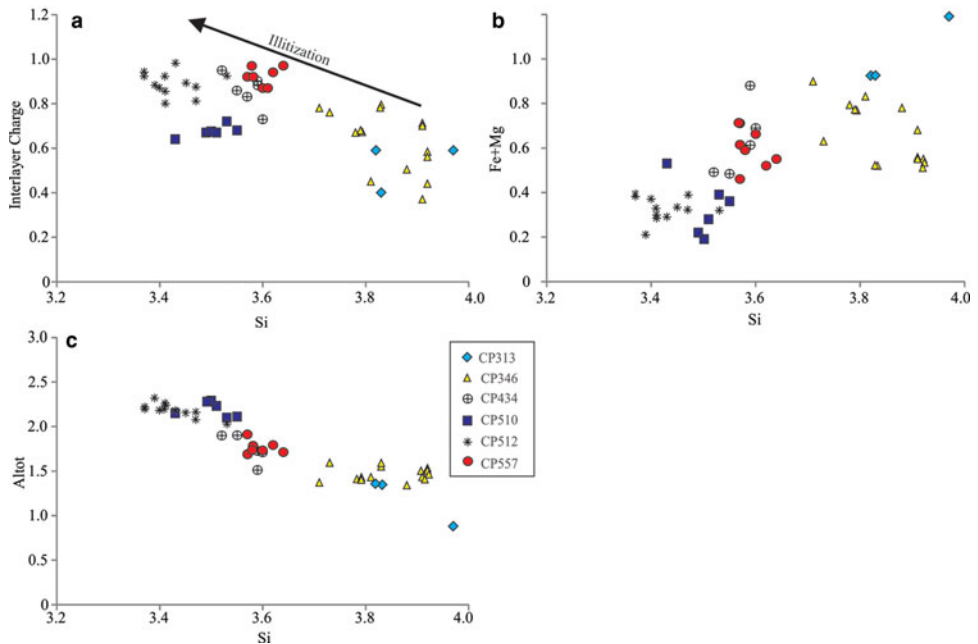


FIG. 10. SEM-EDS analyses of dioctahedral clays on: (a) Si vs. interlayer charge; (b) Si vs. Fe + Mg; and (c) Si vs. total Al diagrams.

argillic zone; (2) sub-propylitic zone; and (3) propylitic zone. The argillic zone mainly affects the shallow part of the system, from 165 m to 315 m in the PexAP-1 well and from 175 m to ~360 m in the CP-1 well. In this interval, an intensive, pervasive alteration dominated by smectite replacing the phenocrysts and the groundmass is observed, associated with hematite, zeolites, calcite and quartz. The smectites mainly have a montmorillonitic composition (Figs 5 and 8; Table 3), typical of smectites associated with the early alteration products of volcanic glass (*e.g.* Bauluz *et al.*, 2002; Guisseau *et al.*, 2007), although some intermediate compositions between montmorillonite and beidellite cannot be ruled out, as is also suggested by XRD analyses (Figs 5, 8). Discrete smectite disappears completely at depths below 345 m, being replaced by I-S. The sub-propylitic zone operates over the depth interval 315–490 m in the PexAP-1 well and over 360–420 m depth in the CP-1 well. This zone is dominated by mixed-layer I-S with R0, R1 and R3 ordering, C-S, corrensite, C-Cor and chlorite, Na-plagioclase, quartz, calcite, hematite, stilbite and laumontite. The amount of expandable layers in I-S and C-Cor decrease with increasing depth and temperature (Table 1, Fig. 13), with random ordered R0 I-S type identified at 345 m depth, and regularly

ordered R1 I-S type at 432–434 m depth. Some exceptions to this trend were observed, as illite-rich R3 I-S appears at ~270 and ~400 m depth (Table 1; Fig. 12). From a depth of 451 m until the propylitic zone (511 m) mixed-layer I-S with R3 ordering dominates. Finally, the propylitic zone, from depths of 490 to 557 m in the PexAP-1 well and from 420 to 825 m in the CP-1 well, is characterized by illite and chlorite as the main phyllosilicates, associated with mixed-layer C-Cor, epidote, Na-plagioclase, adularia, quartz, calcite, pyrite, chalcocopyrite and titanite. The argillic and sub-propylitic zones, dominated mostly by clay minerals, represent a thick clay cap (~300 m thick), while the propylitic zone represents the beginning of the reservoir domain of the Cerro Pabellón geothermal system.

X-ray diffraction analyses and the chemical compositions of smectites, mixed-layer I-S and illites show, with some exceptions, a progressive illitization with depth and through the three alteration zones (smectite → interstratified I-S → illite; Inoue *et al.*, 2004; Meunier & Velde, 1989). This trend is demonstrated by a decrease in Si^{4+} and an increase in interlayer charge with depth, which balances the tetrahedral charge due to the increase in Al^{3+} and decrease in Si^{4+} (Vázquez *et al.*, 2016; Figs 9, 10). However, samples CP273 and

TABLE 4. EDS analyses of trioctahedral phases.

	Si	Al ^{IV}	Al ^{VI}	Fe	Mg	Mn	Ti	Σ oct	K	Na	Ca	Σ int	Al Tot
CP346-1*	5.74	2.26	0.71	3.50	4.97	0.00	0.00	9.18	0.00	0.13	0.20	0.53	2.97
CP346-2*	5.75	2.25	0.78	3.42	5.05	0.00	0.00	9.25	0.00	0.00	0.16	0.32	3.03
CP346-3*	5.78	2.22	0.71	3.62	4.92	0.00	0.00	9.25	0.00	0.00	0.16	0.32	2.93
CP346-4*	5.76	2.24	1.04	3.02	5.16	0.00	0.00	9.22	0.00	0.00	0.09	0.18	3.28
CP434-1*	6.24	1.76	2.88	2.26	2.98	0.00	0.00	8.13	0.19	0.00	0.00	0.19	4.64
CP434-2*	6.57	1.43	3.65	1.47	2.55	0.00	0.00	7.67	0.16	0.00	0.00	0.16	5.08
CP434-3*	5.91	2.09	1.79	2.82	4.22	0.00	0.00	8.83	0.10	0.00	0.00	0.10	3.88
CP434-4*	5.90	2.10	1.79	2.74	4.32	0.00	0.00	8.85	0.08	0.00	0.00	0.08	3.89
CP434-5*	6.07	1.93	2.46	2.35	3.66	0.00	0.00	8.46	0.10	0.00	0.00	0.10	4.39
CP434-6*	6.19	1.81	2.73	1.93	3.52	0.00	0.00	8.17	0.20	0.00	0.09	0.37	4.54
CP434-7*	6.12	1.88	2.61	2.34	3.30	0.00	0.00	8.25	0.00	0.00	0.17	0.34	4.49
CP510-1**	3.29	0.71	1.94	1.41	1.85	0.00	0.00	5.20	0.08	0.00	0.00	0.08	2.66
CP510-2**	3.29	0.71	1.78	1.30	2.25	0.00	0.00	5.33	0.00	0.00	0.00	0.00	2.49
CP510-3**	3.21	0.79	1.97	1.34	1.91	0.00	0.00	5.23	0.09	0.00	0.00	0.09	2.76
CP510-4**	3.27	0.73	1.96	1.39	1.85	0.00	0.00	5.20	0.09	0.00	0.00	0.09	2.68
CP512-1**	3.00	1.00	1.37	2.67	1.20	0.17	0.00	5.41	0.12	0.00	0.08	0.28	2.37
CP512-3**	3.21	0.79	1.59	2.10	1.50	0.12	0.00	5.31	0.17	0.00	0.00	0.17	2.37
CP557-1**	2.88	1.12	0.66	3.15	1.84	0.14	0.00	5.80	0.09	0.00	0.07	0.23	1.78
CP557-2**	2.85	1.15	0.65	3.19	1.86	0.11	0.00	5.82	0.09	0.00	0.07	0.23	1.80
CP557-3**	2.85	1.15	0.40	3.55	1.78	0.16	0.00	5.89	0.00	0.00	0.13	0.26	1.54
CP557-4**	3.01	0.99	0.62	3.36	1.61	0.21	0.00	5.79	0.13	0.00	0.00	0.13	1.61

*C-S and Cor were normalized to O₂₀(OH)₁₀. ** C-Cor and Chl were normalized to O₁₀(OH)₈.

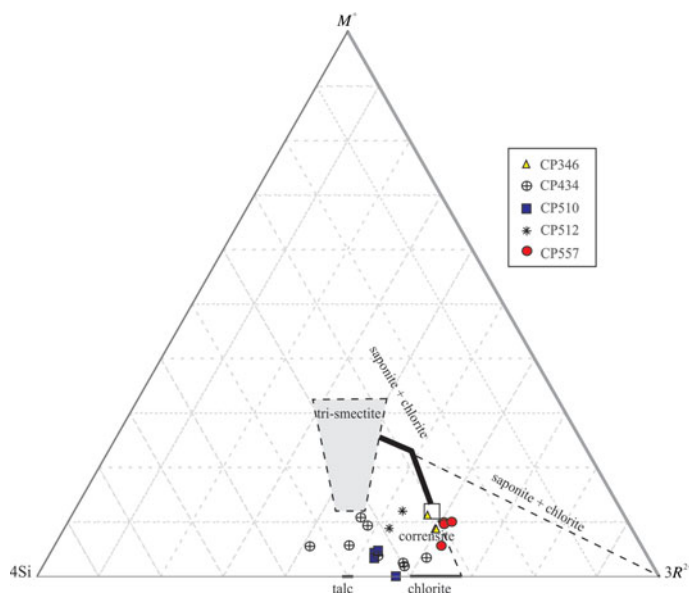


FIG. 11. $M^+-4Si-3R^{2+}$ diagram (Meunier & Velde, 1989) showing the compositional evolution of trioctahedral phases.

CP401 contain R3-type I-S the illite contents of which are not in agreement with the progressive illitization trend. In those samples, R3-type I-S is associated with mixed-layer C-Cor. The illite b -parameter values (~ 8.98 Å) are compatible with the occurrence of dioctahedral clays with low Fe+Mg contents in the deepest levels (see Fig. 10; Moore & Reynolds, 1997; Chemtob *et al.*, 2015), although a slight displacement to higher b parameters (greater Fe+Mg contents) was observed in the bottom of the well (sample CP557; 9.00 Å), in accordance with chemical data (see Fig. 10).

The evolution of trioctahedral clay phases in the PexAP-1 well begins with C-S in the shallower samples down to a depth of 345 m. Down to the bottom of the well, irregular C-S is replaced by corrensite associated with C-Cor with varying proportions of chlorite layers and chlorite between 401 and 434 m. An increase in Fe^{2+} and Al^{3+} contents relative to Mg^{2+} and Si^{4+} , together with the presence of K^+ as the dominant interlayer cation, is associated with these phase transitions. The increase in Fe contents occurs at temperatures >200 °C consistent with other published data (Beaufort *et al.*, 2015 and references therein).

Relationship between measured temperature and clay-mineral distribution

The transition of smectite to illite, *via* mixed-layer I-S has been reported widely in hydrothermal systems

(Harvey & Browne, 1991, 2000; Mas *et al.*, 2006; Vazquez *et al.*, 2014, 2016). On the other hand, the mineral transformation has also been considered to be the result of a thermally activated sequential transformation reaction proceeding *via* crystallization of mixed-layer I-S series (Meunier & Velde, 1989), or the result of simultaneous crystallization of the whole I-S *via* direct precipitation from solution (Inoue *et al.*, 2004). As already mentioned, dioctahedral clay minerals have been used to constrain temperatures in many geothermal systems (Harvey & Browne, 1991; Inoue *et al.*, 2010), as the transition between the two end-member clays involved changes in chemical composition that might be related to temperature.

In geothermal systems, the ranges of temperature recorded for the appearance of smectite, I-S and illite are ~ 75 – 220 °C, ~ 130 – 220 °C and ~ 130 – 300 °C (Wohletz & Heiken, 1992; Day-Stirrat *et al.*, 2010; Vázquez *et al.*, 2014). At Cerro Pabellón, the clay cap consists of the argillic and sub-propylitic zones, characterized by low permeability and temperatures lower than ~ 190 °C. The argillic zone is characterized by the occurrence of clinoptilolite and smectite as index minerals and temperatures between 90 and 175 °C (from depths of 165 to 315 m; Fig. 12). The transition from the argillic to the sub-propylitic zones, with the replacement of smectite for R1 I-S, takes place at 180–185 °C. The sub-propylitic zone (315 and 490 m depth; Fig. 13), characterized by (R1-R3) I-S, is related

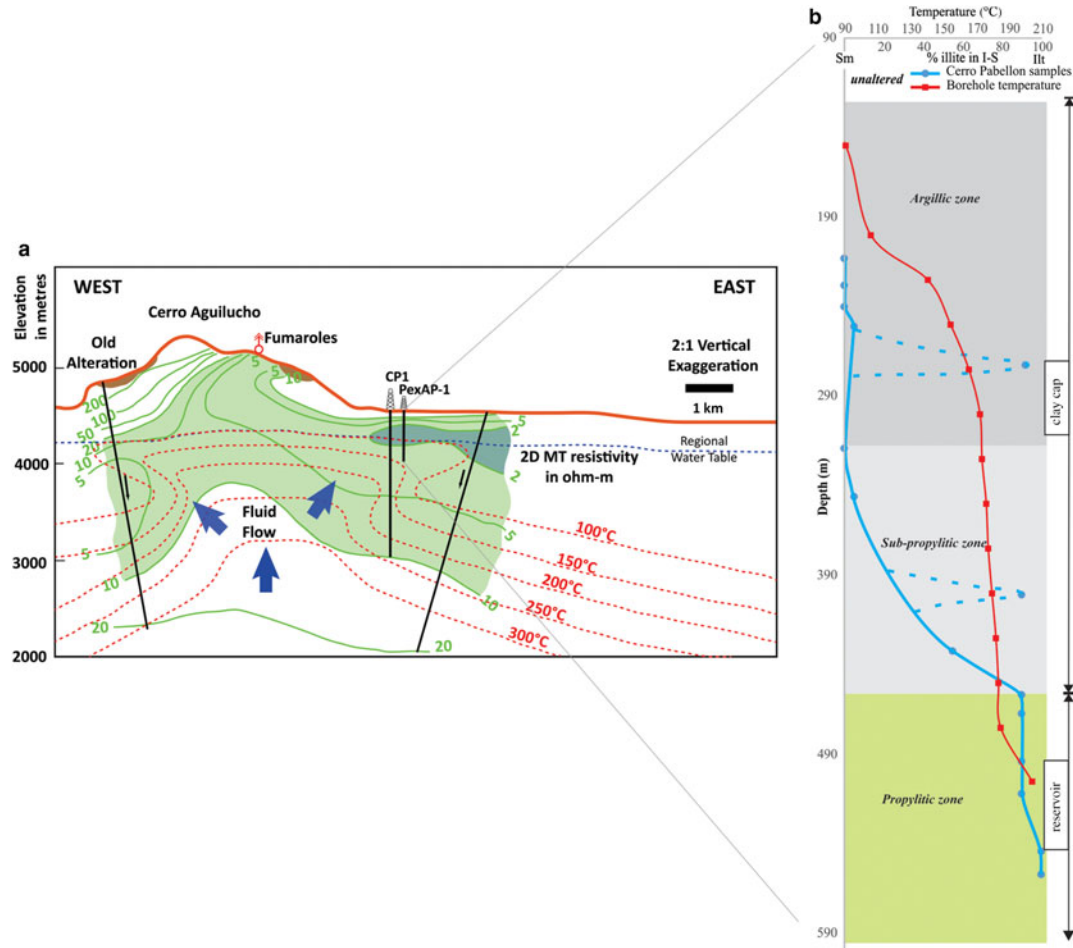


FIG. 12. Simplified conceptual model for the Cerro Pabellón geothermal system: (a) west to east simplified profile of the Cerro Pabellón area showing temperature isotherms and MT (magnetotelluric) resistivity data from Urzúa *et al.* (2002). Following these authors, the <10 ohm-m low resistivity layer was interpreted as a smectite clay cap overlying rocks at temperatures of >200°C as expected over geothermal reservoirs; the lowest (<2 ohm-m) resistivities detected in very shallow smectite clay zones were associated with parched fossil aquifers. (b) Clay-mineral evolution along the clay cap showing the variation in I-S content (blue line) and temperature (red line) along the profile.

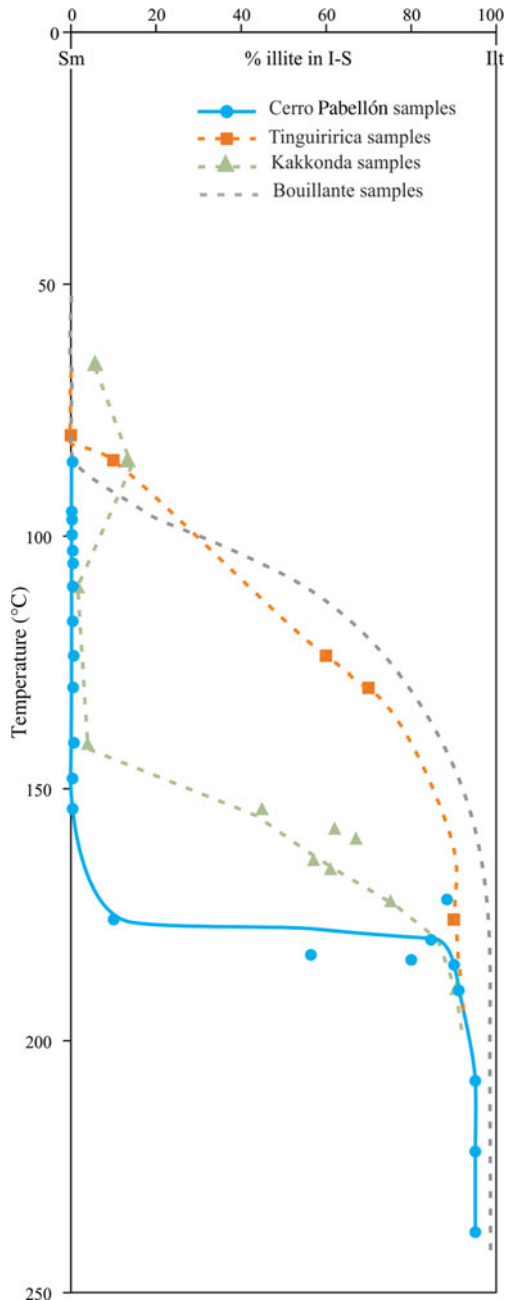


FIG. 13. Variation of % illite in I-S as a function of temperature in PexAP-1 drill core (Cerro Pabellon field), the Tinguiririca (Vázquez *et al.*, 2014), the Bouillante (Mas *et al.*, 2006) and the Kakkonda (Inoue *et al.*, 2004) geothermal fields. Samples CP273 and CP401 are not included within the Cerro Pabellón trend.

to borehole temperatures between 175 and 190°C. Finally, the propylitic zone, with illite (from 490 m downwards), records temperatures >190°C (Fig. 12).

Despite having comparable geothermal gradients, the temperature at which the replacement of smectite for R1 I-S takes place in Cerro Pabellón (180–185°C), is higher than those reported for other similar geothermal fields such as the Tinguiririca geothermal field of Central Chile (80–120°C; Vázquez *et al.*, 2014) and the Bouillante geothermal field of Guadeloupe island (110–160°C; Mas *et al.*, 2006; Fig. 12). Similar temperatures (~180°C) were described for the appearance of R3 I-S in the three geothermal fields. On the other hand, the relationship between the distribution of dioctahedral phases and temperatures in the PexAP-1 well is comparable to those observed in other geothermal systems such as Kakkonda (Japan; Inoue *et al.*, 2004; Fig. 13). These systems are characterized by an abrupt change from smectite to R1 I-S type, with negligible presence of R0 ordering phases (Bethke & Stephen, 1986), showing a sigmoidal variation of the illite layers in I-S.

The different temperatures at which the smectite–R1 I-S transition takes place at Cerro Pabellón, Tinguiririca and Bouillante geothermal fields have been attributed to differences in temperature, fluid composition, fluid/rock ratio, permeability, time, oxygen-activity conditions (f_{O_2}) and chemical composition of the precursor material (Meunier, 2005; Vidal *et al.*, 2016), together with variations in the formation mechanisms. The fluid composition is intimately related to the composition of the rocks (availability of K^+ , Na^+ , Al^{3+} , Si^{4+} ; Inoue *et al.*, 2004). For Cerro Pabellón, Tinguiririca and Bouillante geothermal fields, the XRD bulk-rock analysis and textural study and EDS analysis of samples from the argillic and sub-propylitic zones, show that clay minerals form mainly by direct precipitation from fluids after leaching of K^+ from dissolution of volcanic glass or feldspar, so the availability of K^+ might not explain the recorded differences itself. The observed differences might indicate at least in part, the efficiency of the clay cap in restricting the circulation of fluids of hydrothermal origin. In Cerro Pabellón, the clay cap constitutes a low-permeability environment that is responsible for the absence of surface manifestations. Differences might also be related, at least partially, to the short time interval from the beginning of the hydrothermal processes to the present. Although the influence of time on these systems is controversial (Meunier, 2005; Inoue *et al.*, 2004), the time span during which the illitization processes have been

developed should not be discounted as a possible cause of the different transition temperatures; Ji & Browne (2000) postulated that time may explain the differences observed between the Waitotapu and Ohaaki-Broadlands active geothermal systems in New Zealand that have comparable potassium content and permeability. Inoue *et al.* (2004) also mentioned the influence of short periods on the evolution of hydrothermally altered rocks of geothermal systems.

Wide temperature ranges have been recorded for the presence of trioctahedral phases in geothermal systems. Corrensite has been recorded at between 100 and 200°C (Inoue & Utada, 1991). The complete conversion of corrensite to discrete chlorite is completed above 240°C (Keith & Bargar, 1988; Beaufort *et al.*, 1992; Inoue, 1995). In the case of the PexAP-1 well, corrensite appears at between 172 and 183°C, while the C-Cor and chlorites are present from 180°C. The complete disappearance of corrensite takes place at 183°C. Unlike dioctahedral phases, these temperatures are comparable with those recorded in the Tinguiririca geothermal system, in which the association of low-charge corrensite and discrete chlorite was recorded between 140 and 215°C (Vázquez *et al.*, 2014). This might be attributed to the greater availability of Fe^{2+} and Mg^{2+} relative to K^+ , which are related directly to initial composition of the fluids, lithology and fluid:rock ratios and temperature of the fluids entering the system.

Although the Kübler index was developed as a tool for measuring reaction progress in low-grade metamorphism (see Abad *et al.*, 2006 and Warr & Ferreiro Mahlmann, 2015 for reviews), it was also applied to characterize the clay minerals associated with hydrothermal fields (*cf* McDowell & Elders, 1980; Ji & Browne, 2000; Li *et al.*, 2005; Franchini *et al.*, 2007; Prasetyo *et al.*, 2015; Maydagan *et al.*, 2018). $\text{KI}_{(\text{CIS})}$ values of 0.70°2θ obtained from samples from the propylitic zone are related to borehole temperatures of 220–240°C (interpolated for each depth according to direct temperature measurement in boreholes; Tables 1 and 2). These $\text{KI}_{(\text{CIS})}$ values are comparable with those reported for active geothermal fields in New Zealand ($\text{KI}_{(\text{CIS})}$ values of 0.6–0.71°2θ, Ji & Browne, 2000) and Indonesia (Prasetyo *et al.*, 2015), with temperatures of between 220 and 255°C. In both cases the borehole temperatures are higher than those suggested for the diagenesis to anchizone boundary in burial environments, in which the index was developed (~200°C Merriman & Peacor, 1999). On the other hand, chlorites show Árkai index values which are less than the $\text{KI}_{(\text{CIS})}$ values (Table 2). Although the

geotectonic context is substantially different, similar relationships were recorded for pelites corresponding to zeolite facies from the South Island (New Zealand, Warr & Cox, 2016), which show $\text{KI}_{(\text{CIS})}$ values of 0.52 and 0.32°2θ correlating with Árkai indexes of 0.41 and 0.31°2θ, respectively. In addition to temperature, the availability of K^+ , in the case of illite, and of Mg^{2+} and Fe^{2+} in the case of chlorite, should strongly influence both the reaction paths and rates of crystal growth (Huang *et al.*, 1993; Jahren & Aagaard, 1989).

In the PexAP-1 well two levels at 273 and 400 m containing R3 I-S are outside the observed illitization trend. Sample CP273 belongs to the argillic zone, dominated by smectites, whereas sample CP400 corresponds to the sub-propylitic zone in the transition from R0 to R1 I-S. There is no relationship between the lithological variations in the well and the appearance of R3 I-S at these levels; moreover, the K^+ and Ca^{2+} contents, mainly associated with K-feldspar and calcite, display similar variations throughout the well (Fig. 3). The occurrence of R3 I-S in these levels, >100 m apart on the vertical scale, might be explained by local fluctuations in fluid:rock ratios, mentioned above as a significant variable in the formation of clay minerals. The andesitic levels at which the specific R3 I-S occurs are interlayered in an area dominated by polymictic breccias, possibly leading to zones of greater permeability in the system, associated with hydrostatic fracturing. The veins and fractures described in the drill core are mostly sub-vertical. On the other hand, the brecciation zones would be more susceptible to alteration gradually reducing its permeability and thus the capacity of fluids and heat transmission. It is also possible that these local outflows were developed earlier than the upflows, precisely in these localized andesitic zones favourable for fluids, and thus heat circulation, so the time associated with the mineral transformations would have been longer. A less likely alternative is that these levels represent relics of a higher-temperature, older upflow system, the system currently being in a cooling stage, although there is no clear textural evidence to support this interpretation.

CONCLUSIONS

The blind nature of the Cerro Pabellón geothermal system might be related to the thickness and low permeability of the clay cap (~300 m). Two main clay-minerals reaction series were detected in this clay cap: the smectite to illite and the smectite to chlorite transformations. In fact, the final phases of both

reaction series, illite and chlorite, only prevail in rock samples from the reservoir domain, where mixed-layer I-S and C-S are almost absent. In both reaction series, a continuous and slow reduction of the proportion of smectite layers in mixed layers with depth was observed. The discrepancy observed between increase in temperature with depth and the negligible variation in the mixed-layer I-S in the clay cap might be explained by a kinetic rather than a temperature-controlled reaction progress. The impermeability of the clay cap of the Cerro Pabellón blind geothermal field, would not favour the advance of I-S and C-S reaction series. Thus the replacement of smectite by R1 I-S takes place at ~180–185°C, *i.e.* at higher temperatures than other geothermal fields. In contrast, in the reservoir domain, where permeability is much greater than in the clay cap, the appearance of chlorite and illite really fit with those temperatures recorded in the literature. Detailed study by XRD of clay minerals might help to understand the formation processes of the hydrothermal minerals and how these mineralogical transformations might be controlled not only by temperature (and depth) but also by kinetics related to permeability/porosity that might enhance (or impede) mineral transformations. Consequently, detailed studies of alteration minerals in continuous drill cores should improve the data available for better understanding of the processes that control the development of alteration zones in active geothermal fields and thus the reliability of conceptual models.

ACKNOWLEDGEMENTS

The present study was supported by the Fondap-Conicyt project 15090013 “Centro de Excelencia en Geotermia de Los Andes (CEGA)”. M.T., E.C. and M.P. are grateful for financial support from the University of Urbino (M.T.) and CONICYT (Chile, E.C. & M.P.) for their respective, PhD grants. G.C. acknowledges financial support from PUE 2016 - CONICET – CICTERRA and ANPCyT. The authors are particularly grateful to Guido Cappetti (Geotérmica del Norte – GDN- and ENEL Green Power Chile) for provision of the facilities used to carry out this study and for samples of the exploratory drill-core material. Reviews by Margarita DoCampo, Fernando Nieto and an anonymous reviewer are also acknowledged sincerely; they helped to improve this work.

REFERENCES

Abad I., Nieto F., Gutierrez-Alonso G., Do Campo M., Lopez-Munguira A. & Velilla N. (2006) Illitic substitution in micas of very low-grade metamorphic

clastic rocks. *European Journal of Mineralogy*, **18**, 59–69.

- Ahumada S. & Mercado J.L. (2009) *Evolución geológica y estructural del complejo volcánico Apacheta-Aguilucho (CVAA), Segunda Región, Chile*. Dissertation, Bachelor's Degree Thesis, Universidad Católica del Norte, Antofagasta, Chile.
- Aravena D., Muñoz M., Morata D., Lahsen A., Parada M. A. & Dobson P. (2016) Assessment of high enthalpy geothermal resources and promising areas of Chile. *Geothermics*, **59**, 1–13.
- Artemieva I.M., editor (2011) *The Lithosphere: An Interdisciplinary Approach*. Cambridge University Press, UK, 794 pp.
- Bauluz B., Peacor D.R. & Ylagan R.F. (2002) Transmission electron microscopy study of smectite illitization during hydrothermal alteration of a rhyolitic hyaloclastite from Ponzá, Italy. *Clays and Clay Minerals*, **50** (2), 157–173.
- Beaufort D., Patrier P., Meunier A. & Ottaviani M.M. (1992) Chemical variations in assemblages including epidote and/or chlorite in the fossil hydrothermal system of Saint Martin (Lesser Antilles). *Journal of Volcanology and Geothermal Research*, **51**, 95–114.
- Beaufort D., Baronnet A., Lanson B. & Meunier A. (1997) Corrensite: A single phase or a mixed-layer phyllosilicate in the saponite-to-chlorite conversion series? A case study of Sancerre-Couy deep drill hole (France). *American Mineralogist*, **82**, 109–124.
- Beaufort D., Rigault C., Billon S., Billault V., Inoue A., Inoue S., Patrier P. & Ferrage E. (2015) Chlorite and chloritization processes through mixed-layer mineral series in low-temperature geological systems – a review. *Clay Minerals*, **50**, 497–523.
- Bethke C.M. & Stephen P.A. (1986) Layer-by-layer mechanism of smectite illitization and application to a new rate law. *Clays and Clay Minerals*, **34**, 136–145.
- Brasse H., Lezaeta P., Rath V., Schwalenberg K., Soyer W. & Haak V. (2002) The Bolivian Altiplano conductivity anomaly. *Journal of Geophysical Research*, **107**, 2096.
- Charrier R., Pinto L. & Rodríguez M.P. (2007) Tectonostratigraphic evolution of the Andean Orogen in Chile. Pp. 21–114 in: *The Geology of Chile* (T. Moreno & W. Gibbons, editors). ‘Geology of Series’, Geological Society London.
- Chemtob S.M., Nickerson R.D., Morris R.V., Agresti D. G. & Catalano J.G. (2015) Synthesis and structural characterization of ferrous trioctahedral smectites: Implications for clay mineral genesis and detectability on Mars. *Journal of Geophysical Research: Planets*, **120**, 1119–1140.
- Corrado S., Aldega L., Celano A.S., de Benedetti A.A. & Giordano G. (2014) Cap rock efficiency and fluid circulation of natural hydrothermal systems by means of XRD on clay minerals (Sutri, northern Latium, Italy). *Geothermics*, **50**, 180–188.

- Day-Stirrat R.J., Dutton S.P., Milliken K.L., Loucks R.G., Aplin A.C., Hillier S. & van der Pluijm B.A. (2010) Fabric anisotropy induced by primary depositional variations in the silt: clay ratio in two fine-grained slope fan complexes: Texas Gulf Coast and northern North Sea. *Sedimentary Geology*, **226**, 42–53.
- de Silva S.L. (1989) Altiplano-Puna volcanic complex of the central Andes. *Geology*, **17**, 1102–1106.
- de Silva S.L. & Gosnold W.D. (2007) Episodic construction of batholiths: Insights from the spatiotemporal development of an ignimbrite flare-up. *Journal of Volcanology and Geothermal Research*, **167**, 320–335.
- Fariás M., Charrier R., Comte D., Martinod J. & Hérail G. (2005) Late Cenozoic deformation and uplift of the western flank of the Altiplano: Evidence from the depositional, tectonic, and geomorphologic evolution and shallow seismic activity (northern Chile at 19°30' S). *Tectonics*, **24**, 1–27.
- Franchini M., Impiccini A., Meinert L., Grathoff G. & Schalamuk I.B.A. (2007) Clay mineralogy and zonation in the Campana Mahuida porphyry Cu deposit, Neuquén, Argentina: Implications for porphyry Cu exploration. *Economic Geology*, **102**, 27–54.
- Francis P.W. & Rundle C.C. (1976) Rates of production of the main magma types in the central Andes. *Geological Society of America Bulletin*, **87**, 474–480.
- Gifkins C., Herrmann W. & Large R. (editors) (2005) *Altered Volcanic Rocks – A Guide to Description and Interpretation*. Centre for Ore Deposit Research, University of Tasmania, Hobart, 288 pp.
- Guidotti C.V., Yates M.G., Dyar M.D. & Taylor M.E. (1994) Petrogenetic implications of the Fe³⁺ contents of muscovite in pelitic schists. *American Mineralogist*, **79**, 793–795.
- Guisseau D., Patrier-Mas P., Beaufort D., Girard J.P., Inoue A., Sanjuan B., Petit S., Lens A. & Genter A. (2007) Significance of the depth-related transition montmorillonite-beidellite in the Bouillante geothermal field (Guadeloupe, Lesser Antilles). *American Mineralogist*, **92**, 1800–1813.
- Godoy B., Rodríguez I., Pizarro M. & Rivera G. (2017) Geomorphology, lithofacies, and block characteristics to determine the origin, and mobility, of a debris avalanche deposit at Apacheta-Aguilucho Volcanic Complex (AAVC), northern Chile. *Journal of Volcanology and Geothermal Research*, doi:
- González G., Cembrano J., Carrizo D., Macci A. & Schneider H. (2003) The link between forearc tectonics and Pliocene-Quaternary deformation of the Coastal cordillera, northern Chile. *Journal of South American Earth Sciences*, **16**, 321–342.
- Harrison W.E., Luza K.V., Prater M.L. & Chueng P.K. (1983) *Geothermal resource assessment of Oklahoma*. Special Publication, Oklahoma Geological Survey, 83–1.
- Harvey C.C. & Browne P.R.I. (1991) Mixed-layer clay geothermometry in the Wairakei geothermal field, New Zealand. *Clay and Clay Minerals*, **39**, 614–621.
- Harvey C.C. & Browne P.R.I. (2000) Studies of mixed-layer clays in geothermal systems. A review of the developments and their effectiveness as mineral geothermometers. *Proceeding of the World Geothermal Congress, Japan*.
- Herrera S., Pinto L., Deckart K., Cortés J. & Valenzuela I. (2017) Cenozoic tectonostratigraphic evolution and architecture of the Central Andes in northern Chile based on the Aquine region, Western Cordillera (19–19°30' S). *Andean Geology*, **44**, 87–122.
- Huang W.L., Longo J.M. & Pevear D.R. (1993) An experimentally derived kinetic model for smectite-to-illite conversion and its use as a geothermometer. *Clays and Clay Minerals*, **41**, 162–177.
- Inoue A. (1995) Formation of clay minerals in hydrothermal environments. Pp. 268–329 in: *Origin and Mineralogy of Clays* (B. Velde, editor). Springer, Berlin, Heidelberg.
- Inoué S. & Kogure T. (2016) High-angle annular dark field scanning transmission electron microscopic (HAADF-STEM) study of Fe-rich 7 Å–14 Å interstratified minerals from a hydrothermal deposit. *Clay Minerals*, **51**, 603–613.
- Inoue A. & Utada M. (1991) Smectite-to-chlorite transformation in thermally metamorphosed and volcanoclastic rocks in the Kamikita area, northern Honshu, Japan. *American Mineralogist*, **76**, 628–640.
- Inoue A., Meunier A. & Beaufort D. (2004) Illite-smectite mixed-layer minerals in felsic volcanoclastic rocks from drill cores, Kakkonda, Japan. *Clays and Clay Minerals*, **52**, 66–84.
- Inoue A., Kurokawa K. & Hata T. (2010) Application of chlorite geothermometry to hydrothermal alteration in Toyoha Geothermal System, southwestern Hokkaido, Japan. *Resource Geology*, **60**, 52–70.
- Jahren J.S. & Aagaard P. (1989) Compositional variations in diagenetic chlorites and illites, and relationships with formation-water chemistry. *Clay Minerals*, **24**, 157–170.
- Ji J. & Browne P.R.J. (2000) Relationship between illite crystallinity and temperature in active geothermal systems of New Zealand. *Clay and Clay Minerals*, **48**, 139–144.
- Keith T.E.C. & Bargar I.C.E. (1988) Petrology and hydrothermal mineralogy of U.S. Geological Survey Newberry 2 drill core from Newberry caldera, Oregon. *Journal of Geophysical Research*, **93**, 10174–10190.
- Kisch H.J. (1991) Illite crystallinity: recommendations on sample preparation, X-ray diffraction settings, and interlaboratory samples. *Journal of Metamorphic Geology*, **9**, 665–670.
- Kübler B. (1968) Evaluation quantitative du métamorphisme par la cristallinité d'illite. *Bulletin de la Centre Recherche de Pau – S.N.P.A.*, **2**, 385–397.
- Lahsen A. (1988) Chilean geothermal resources and their possible utilization. *Geothermics*, **17**, 401–410.
- Lahsen A. & Trujillo P. (1975) El Tatio geothermal field. *Proceedings of the Second United Nations Symposium*

- on the Development and Use of Geothermal Resources, pp. 157–178.
- Li X., Wang C., Mao J., Hua R., Liu Y. & Xu Q. (2005) Kübler Index and K-Ar ages of illite in the Yinshan Polymetallic Deposit, Jiangxi Province, South China: Analyses and implications. *Resource Geology*, **55**, 397–404.
- Maffucci R., Corrado S., Aldega L., Bigi S., Chiodi A., Di Paolo L. & Invernizzi C. (2016) Cap rock efficiency of geothermal systems in fold-and-thrust belts: Evidence from paleo-thermal and structural analyses in Rosario de La Frontera geothermal area (NW Argentina). *Journal of Volcanology and Geothermal Research*, **328**, 84–95.
- Marinović N. & Lahsen A. (1984) Carta geológica de Chile No. 58: Hoja Calama, Región de Antofagasta.
- Mas A., Guisseau D., Patrier Mas P., Beaufort D., Genter A., Sanjuan B. & Girard J.P. (2006) Clay minerals related to the hydrothermal activity of the Bouillante geothermal field (Guadeloupe). *Journal of Volcanology and Geothermal Research*, **158**, 380–400.
- Maydagan L., Franchini M., Impiccini A., Lentz D., Patrier P. & Beaufort D. (2018) Chlorite, white mica and clay minerals as proximity indicators to ore in the shallow porphyry environment of Quebrada de la Mina deposit, Argentina. *Ore Geology Reviews*, **92**, 297–317.
- McDowell S.D. & Elders W.A. (1980) Authigenic layer silicate minerals in borehole Elmore 1, Salton Sea geothermal field, California, USA. *Contributions to Mineralogy and Petrology*, **74**, 293–310.
- Merriman R.J. & Peacor D.R. (1999) Very low-grade metapelites; mineralogy, microfabrics and measuring reaction progress. Pp. 10–60 in: *Low-grade Metamorphism* (M. Frey & D. Robinson, editors). Blackwell Sciences Ltd., Oxford, UK.
- Meunier A. (2005) Hydrothermal process – thermal metamorphism. Pp. 379–415 in: *Clays* (A. Meunier, editor). Springer Science & Business Media, Berlin.
- Meunier A. & Velde B. (1989) Solid solution in illite/smectite mixed layer minerals and illite. *American Mineralogist*, **74**, 1106–1112.
- Meunier A., Mas A., Beaufort D., Patrier P. & Dudoignon P. (2008a) Clay minerals in basalt-hawaiite rocks from Mururoa atoll (French Polynesia). I. Mineralogy. *Clays and Clay Minerals*, **56**, 711–729.
- Meunier A., Mas A., Beaufort D., Patrier P. & Dudoignon P. (2008b) Clay minerals in basalt-hawaiite rocks from Mururoa atoll (French Polynesia). II. Petrography and geochemistry. *Clays and Clay Minerals*, **56**, 730–750.
- Moore D.M. & Reynolds Jr R.C., editors (1997) *X-ray Diffraction and the Identification and Analysis of Clay Minerals*. 2nd edition. Oxford University Press, New York, 378 pp.
- Nieto F. (1997). Chemical composition of metapelitic chlorites: X-ray diffraction and optical property approach. *European Journal of Mineralogy*, **9**, 829–841.
- Piscaglia F. (2012) The high temperature geothermal field of the Apacheta-Aguilucho Volcanic Complex (northern Chile): Geo-petrographic surface exploration, crustal heat sources and cap-rocks. *Plinius*, **38**, 148–153.
- Prasetyo I., Sardiyo, Koestono H. & Thamrin M.H. (2015) Clay alteration study from wells of Tompasso Geothermal Field, north Sulawesi, Indonesia. *Proceedings World Geothermal Congress 2015*, 1–9.
- Ramírez C.F. & Huete C. (1981) Carta Geológica de Chile, Hoja Ollagüe, Escala 1:250,000. *Instituto de Investigaciones Geológicas, Carta No. 40*.
- Renzulli A., Menna M., Tibaldi A. & Flude S. (2006) New data of surface geology, petrology and Ar-Ar geochronology of the Altiplano-Puna Volcanic Complex (Northern Chile) in the framework of future geothermal exploration. *Congreso Geológico Chileno N° 11 Actas*, pp. 307–310.
- Rivera G., Morata D. & Ramírez C. (2015) Evolución vulcanológica y tectónica del área del Cordón Volcánico Cerro del Azufre – Cerro de Inacaliri y su relación con el Sistema Geotérmico de Pampa Apacheta, II Región de Antofagasta. *Congreso Geológico Chileno N° 14 Actas*, pp. 556–559.
- Sánchez-Alfaro P., Sielfeld G., van Campen B., Dobson P., Fuentes V., Reed A., Palma-Behnke R. & Morata D. (2015) Geothermal barriers, policies and economics in Chile – Lessons for the Andes. *Renewable and Sustainable Energy Reviews*, **51**, 1390–1401.
- Sánchez-Alfaro P., Reich M., Arancibia G., Pérez-Flores P., Cembrano J., Driesner T., Lizama M., Rowland J., Morata D., Heinrich C.A., Tardani D. & Campos D. (2016) Physical, chemical and mineralogical evolution of the Tolhuaca geothermal system, southern Andes, Chile: Insights into the interplay between hydrothermal alteration and brittle deformation. *Journal of Volcanology and Geothermal Research*, **324**, 88–104.
- Schmitz M., Lessel K., Giese P., Wigger P., Araneda M., Bribach J., Graeber F., Grunewald S., Haberland C., Lüth S., Röwer P., Ryberg T. & Schulze A. (1999) The crystal structure beneath the central Andean forearc and magmatic arc as derived from seismic studies – the PISCO 94 experiment in northern Chile (21°–23°S). *Journal of South American Earth Sciences*, **12**, 237–260.
- Springer M. & Förster A. (1998) Heat-flow density across the Central Andean subduction zone. *Tectonophysics*, **29**, 123–139.
- Środoń J. (1981) X-ray identification of randomly interstratified illite-smectite in mixtures with discrete illite. *Clay Minerals*, **16**, 297–304.

- Stimac J., Goff F. & Goff C. (2015) Intrusion-related geothermal systems. Pp. 799–822 in: *The Encyclopedia of Volcanoes*. Elsevier, Amsterdam.
- Tassi F., Aguilera F., Darrah T., Vaselli O., Capaccioni B., Poreda R.J. & Delgado-Huertas A. (2010) Fluid geochemistry of hydrothermal systems in the Arica-Parinacota, Tarapacá and Antofagasta regions (northern Chile). *Journal of Volcanology and Geothermal Research*, **192**, 1–15.
- Tibaldi A., Corazzato C. & Rovida A. (2009) Miocene–Quaternary structural evolution of the Uyuni–Atacama region, Andes of Chile and Bolivia. *Tectonophysics*, **471**, 114–135.
- Tibaldi A., Bonali F.L. & Corazzato C. (2016) Structural control on volcanoes and magma paths from local- to orogen-scale: The central Andes case. *Tectonophysics*, **699**, 16–41.
- Tierney C.R., Schmitt A.K., Lovera O.M. & de Silva S.L. (2016) Voluminous plutonism during volcanic quiescence revealed by thermochemical modeling of zircon. *Geology*, **44**, 683–686.
- Todesco M. & Giordano G. (2010) Modelling of CO₂ circulation in the Colli Abani area. Pp. 311–330 in: *The Colli Albano Volcano* (R. Funicello & G. Giordano, editors). Special Publication of IAVCEI, **3**. The Geological Society, London.
- Trumbull R., Riller U., Oncken O., Scheuber E., Munier K. & Hongn F. (2006) The time space distribution of Cenozoic volcanism in the South-Central Andes: a new data compilation and some tectonic implications. Pp. 29–43 in: *The Andes Active Subduction Orogeny, Frontiers in Earth Sciences* (O. Oncken, G. Chong, G. Franz, P. Giese, H.J. Götze, V.A. Ramos, M.R. Strecker, P. Wigger, editors). Springer, Heidelberg, Berlin.
- Urzúa L., Powell T., Cumming W.B. & Dobson P. (2002) Apacheta, a new geothermal prospect in Northern Chile. *Geothermal Resources Council Transactions*, **26**, 22–25.
- Vázquez M., Nieto F., Morata D., Droguett B., Carrillo-Rosúa F.J. & Morales S. (2014) Evolution of clay mineral assemblages in the Tinguiririca geothermal field, Andean Cordillera of central Chile: an XRD and HRTEM-AEM study. *Journal of Volcanology and Geothermal Research*, **282**, 43–59.
- Vázquez M., Bauluz B., Nieto F. & Morata D. (2016) Illitization sequence controlled by temperature in volcanic geothermal systems: The Tinguiririca geothermal field, Andean Cordillera, Central Chile. *Applied Clay Science*, **134**, 221–234.
- Velde B. (1985) *Clay Minerals: A Physico-Chemical Explanation of their Occurrence*. Elsevier, Amsterdam and New York.
- Vidal O., Lanari P., Munoz M., Bourdelle F. & Andrade V. (2016) Deciphering temperature, pressure and oxygen-activity conditions of chlorite formation. *Clay Minerals*, **51**, 615–633.
- Ward K.M., Zandt G., Beck S.L., Christensen D.H. & McFarlin H. (2014) Seismic imaging of the magmatic underpinnings beneath the Altiplano-Puna volcanic complex from the joint inversion of surface wave dispersion and receiver functions. *Earth and Planetary Science Letters*, **404**, 43–53.
- Warr L.N. & Cox S.C. (2016) Correlating illite (Kübler) and chlorite (Árkai) “crystallinity” indices with metamorphic mineral zones of the South Island, New Zealand. *Applied Clay Science*, **134**, 164–174.
- Warr L.N. (2017) On the availability of clay mineral “crystallinity” index standards. 16th International Clay Conference, Granada, Spain.
- Warr L.N. & Ferreiro Mahlmann R.F. (2015) Recommendations for Kübler Index standardization. *Clay Minerals*, **50**, 283–286.
- Warr L.N. & Rice H.N. (1994) Interlaboratory standardization and calibration of clay mineral crystallinity and crystallite size data. *Journal of Metamorphic Geology*, **12**, 141–152.
- Wohletz K. & Heiken G. (1992) *Volcanology and Geothermal Energy*. University of California Press, Berkeley, California, USA, 432 pp.
- Zandt G., Leidig M., Chmielowski J., Baumont D. & Yuan X. (2003) Seismic detection and characterization of the Altiplano-Puna magma body, Central Andes. *Pure and Applied Geophysics*, **160**, 789–807.